



# Nav1.2 and BK channel interaction shapes the action potential in the axon initial segment

Luiza Filipis, Laila Ananda Blömer, Jérôme Montnach, Gildas Loussouarn, Michel de Waard, Marco Canepari

## ► To cite this version:

Luiza Filipis, Laila Ananda Blömer, Jérôme Montnach, Gildas Loussouarn, Michel de Waard, et al.. Nav1.2 and BK channel interaction shapes the action potential in the axon initial segment. The Journal of Physiology, 2023, 601 (10), pp.1957-1979. 10.1113/JP283801 . hal-04235449

**HAL Id: hal-04235449**



**<https://nantes-universite.hal.science/hal-04235449>**

Submitted on 10 Oct 2023

**HAL** is a multi-disciplinary open access archive for the deposit and dissemination of scientific research documents, whether they are published or not. The documents may come from teaching and research institutions in France or abroad, or from public or private research centers.

L'archive ouverte pluridisciplinaire **HAL**, est destinée au dépôt et à la diffusion de documents scientifiques de niveau recherche, publiés ou non, émanant des établissements d'enseignement et de recherche français ou étrangers, des laboratoires publics ou privés.

# Nav1.2 and BK channel interaction shapes the action potential in the axon initial segment

Luiza Filipis<sup>1,2</sup> , Laila Ananda Blömer<sup>1,2</sup>, Jérôme Montnach<sup>2,3</sup>, Gildas Loussouarn<sup>2,3</sup>, Michel De Waard<sup>2,3</sup> and Marco Canepari<sup>1,2,4</sup> 

<sup>1</sup>University Grenoble Alpes, CNRS, LIPhy, Grenoble, France

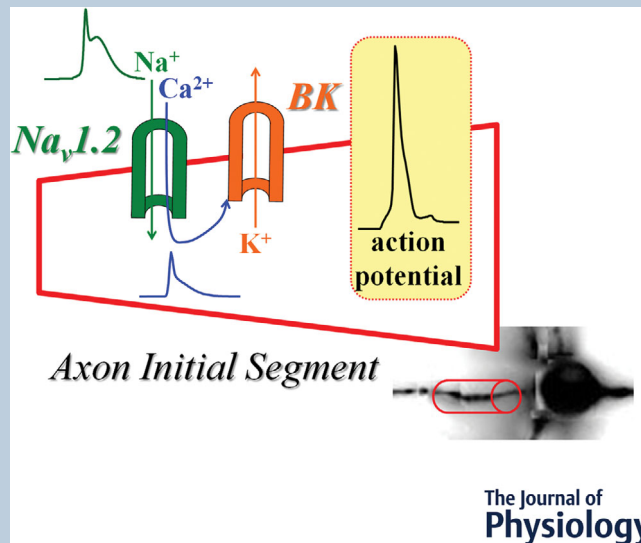
<sup>2</sup>Laboratories of Excellence, Ion Channel Science and Therapeutics, Valbonne, France

<sup>3</sup>Nantes Université, CNRS, INSERM, l'Institut du Thorax, Nantes, France

<sup>4</sup>Institut National de la Santé et Recherche Médicale, Paris, France

Handling Editors: Katalin Toth & Jean-Claude Béïque

The peer review history is available in the Supporting Information section of this article (<https://doi.org/10.1113/JP283801#support-information-section>).



**Abstract** In neocortical layer-5 pyramidal neurons, the action potential (AP) is generated in the axon initial segment (AIS) when the membrane potential ( $V_m$ ) reaches the threshold for activation of

**Luiza Filipis** has been a postdoctoral fellow at the Laboratory of Interdisciplinary Physics in Grenoble (France) where she also obtained her PhD in Life Physics. She was previously at Athens University (Greece) where she studied Nuclear and Medical Physics before pursuing her Masters in Biophysics at the University of Grenoble Alpes (France). Her research has focused on sodium signalling in the axon initial segment explored at high spatiotemporal resolution. **Laila Ananda Blömer** obtained her PhD at the Laboratory of Interdisciplinary Physics in Grenoble (France) where she defended her thesis in December 2022. She completed her master's degree in Brain & Mind Sciences at University College London (UK), after obtaining her interdisciplinary bachelor's degree at the University of Amsterdam (The Netherlands). In her research, she is interested in combining various experimental and computational tools to study neuronal action potential propagation in health and disease.



L. Filipis and L. A. Blömer contributed equally to this work.

This article was first published as a preprint. Filipis L, Blömer LA, Montnach J, De Waard M, Canepari M. 2022. Nav1.2 and BK channels interaction shapes the action potential in the axon initial segment. bioRxiv. <https://doi.org/10.1101/2022.04.12.488116>

the voltage-gated Na<sup>+</sup> channels (VGNCs) Na<sub>v</sub>1.2 and Na<sub>v</sub>1.6. Yet, whereas these VGNCs are known to differ in spatial distribution along the AIS and in biophysical properties, our understanding of the functional differences between the two channels remains elusive. Here, using ultrafast Na<sup>+</sup>, V<sub>m</sub> and Ca<sup>2+</sup> imaging in combination with partial block of Na<sub>v</sub>1.2 by the peptide G<sup>1</sup>G<sup>4</sup>-huwentoxin-IV, we demonstrate an exclusive role of Na<sub>v</sub>1.2 in shaping the generating AP. Precisely, we show that selective block of ~30% of Na<sub>v</sub>1.2 widens the AP in the distal part of the AIS and we demonstrate that this effect is due to a loss of activation of BK Ca<sup>2+</sup>-activated K<sup>+</sup> channels (CAKCs). Indeed, Ca<sup>2+</sup> influx via Na<sub>v</sub>1.2 activates BK CAKCs, determining the amplitude and the early phase of repolarization of the AP in the AIS. By using control experiments using 4,9-anhydrotetrodotoxin, a moderately selective inhibitor of Na<sub>v</sub>1.6, we concluded that the Ca<sup>2+</sup> influx shaping the early phase of the AP is exclusive of Na<sub>v</sub>1.2. Hence, we mimicked this result with a neuron model in which the role of the different ion channels tested reproduced the experimental evidence. The exclusive role of Na<sub>v</sub>1.2 reported here is important for understanding the physiology and pathology of neuronal excitability.

(Received 2 September 2022; accepted after revision 15 March 2023; first published online 23 March 2023)

**Corresponding author** Marco Canepari: Laboratoire Interdisciplinaire de Physique (UMR 5588), Bat. E45, 140 avenue de la physique, Domaine univ., 38402 St Martin d'Hères cedex, France. Email: marco.canepari@univ-grenoble-alpes.fr

**Abstract figure legend** In the axon initial segment of neocortical pyramidal neurons the voltage-gated Na<sup>+</sup> channel Na<sub>v</sub>1.2 contributes to the generation of the action potential by providing an Na<sup>+</sup> current and a Ca<sup>2+</sup> current that activates BK Ca<sup>2+</sup>-activated K<sup>+</sup> channels, shaping the kinetics of the action potential.

### Key points

- We optically analysed the action potential generated in the axon initial segment of mouse layer-5 neocortical pyramidal neurons and its associated Na<sup>+</sup> and Ca<sup>2+</sup> currents using ultrafast imaging techniques.
- We found that partial selective block of the voltage-gated Na<sup>+</sup> channel Na<sub>v</sub>1.2, produced by a recently developed peptide, widens the shape of the action potential in the distal part of the axon initial segment.
- We demonstrate that this effect is due to a reduction of the Ca<sup>2+</sup> influx through Na<sub>v</sub>1.2 that activates BK Ca<sup>2+</sup>-activated K<sup>+</sup> channels.
- To validate our conclusions, we generated a neuron model that reproduces the ensemble of our experimental results.
- The present results indicate a specific role of Na<sub>v</sub>1.2 in the axon initial segment for shaping of the action potential during its generation.

## Introduction

In most mammalian neurons, the action potential (AP) is generated in the axon initial segment (AIS) where its waveform is shaped (Leterrier, 2016). The build-up of the AP waveform in the AIS is the result of the sequential activation, inactivation and de-activation of diverse voltage-gated ion channels (Bean, 2007), starting from activation of voltage-gated Na<sup>+</sup> channels (VGNCs). In the AIS of excitatory pyramidal neurons, Na<sub>v</sub>1.2 and Na<sub>v</sub>1.6 are the two isoforms of VGNCs present (Tian et al., 2014), and understanding the functional role of

these two channels is therefore crucial to link the AP shape to the later sequence of ion-channel activation and de-activation steps. Specifically, in neocortical layer-5 (L5) pyramidal neurons, these two channels have different axonal distributions (Hu et al., 2009) and biophysical properties (Rush et al., 2005). The Na<sup>+</sup> current associated with the AP is characterized by a fast inactivating component and by a non-inactivating component (Astman et al., 2006). Na<sub>v</sub>1.6-deficient mice are characterized by a reduced non-inactivating Na<sup>+</sup> current (Katz et al., 2018), whereas Na<sub>v</sub>1.2-deficient mice are characterized by reduced dendritic excitability and

synaptic function (Spratt et al., 2019). Furthermore,  $\text{Na}_v1.2$  channels are also permeable to  $\text{Ca}^{2+}$  and mediate  $\text{Ca}^{2+}$  influx in the AIS during the AP (Hanemaaijer et al., 2020). However, the precise native role of  $\text{Na}_v1.2$  and  $\text{Na}_v1.6$  and their contributions to generation of the AP remain to be understood. Importantly, channelopathies of  $\text{Na}_v1.2$  (Hedrich et al., 2019) and  $\text{Na}_v1.6$  (Menezes et al., 2020) are the cause of severe neuronal disorders, and shedding light on the role of these two channels is important to tackle these genetic pathologies.

Until recently, study of the activation and signalling of one specific VGNC isoform has been limited by a series of experimental obstacles. First, unambiguous discrimination between  $\text{Na}_v1.2$  and  $\text{Na}_v1.6$  has not been achieved until now with present pharmacological tools. Second, the inhomogeneous distribution of VGNCs and the site-dependence of the AP waveform require recording ion concentrations and membrane potential ( $V_m$ ) transients at high spatial and temporal resolution for proper understanding of the role of each channel subtype. Finally, the change in  $V_m$  transients induced by VGNC inhibition affects the activation of the other voltage-gated ion channels involved in AP shaping. In this study, we tackled all these challenges and analysed the role of native  $\text{Na}_v1.2$  in the generation of the AP, by obtaining a partial but selective and stable effect on  $\text{Na}_v1.2$ , with respect to  $\text{Na}_v1.6$ , with a peptide mutated from a wild-type animal toxin. In the AIS of L5 pyramidal neurons, without distinguishing between L5a and L5b cells, we optically measured  $\text{Na}^+$  currents (Filipis & Canepari, 2021),  $V_m$  transients (Popovic et al., 2015) and  $\text{Ca}^{2+}$  currents (Ait Ouares et al., 2016; Jaafari & Canepari, 2016; Jaafari et al., 2014; Jaafari et al., 2015) associated with APs elicited by somatic current injection and we analysed how the partial block of  $\text{Na}_v1.2$  affected these signals. We then focused on the changes in these signals produced by fully blocking voltage-gated  $\text{Ca}^{2+}$  channels (VGCCs) and/or  $\text{Ca}^{2+}$ -activated  $\text{K}^+$  channels (CAKCs) to correlate  $\text{Na}_v1.2$  signalling with the activation of these channels. To assess whether the role of  $\text{Na}_v1.2$  was exclusive, we performed control experiments using a partially selective  $\text{Na}_v1.6$  inhibitor. Finally, to reconstruct the sequence of activation of the channels underlying shaping of the generating AP, we built a neuron model starting from existing models of the AIS of L5 pyramidal neurons (Baranauskas et al., 2013; Cohen et al., 2020; Fleidervish et al., 2010; Hallermann et al., 2012; Hanemaaijer et al., 2020; Hu et al., 2009; Kole et al., 2008), available in the NeuroDB database. As already done in another system (Ait Ouares et al., 2019), we reproduced the experimental profiles of ionic and  $V_m$  transients and their modifications following selective blocks of individual channel types, in this way mimicking the experimental effects of partially blocking  $\text{Na}_v1.2$  in the AIS.

## Methods

### Ethical approval

Experiments in brain slices were performed at the Laboratory of Interdisciplinary Physics in Grenoble in accordance with European Directives 2010/63/UE on the care, welfare and treatment of animals. Procedures were reviewed by the ethics committee affiliated to the animal facility of the university (D3842110001). These conformed to the ethical principles of the *Journal of Physiology*.

### Selectivity tests of $\text{G}^1\text{G}^4$ -huwentoxin-IV and of 4,9-anhydrotetrodotoxin

Preliminary data on  $\text{G}^1\text{G}^4$ -huwentoxin-IV (hwtx), without analysis of its selectivity, were previously reported (Lopez et al., 2021). Tests of the selectivity of hwtx and 4,9-anhydrotetrodotoxin (atx) were performed on HEK293 cells stably expressing either  $\text{Na}_v1.2$  or  $\text{Na}_v1.6$  channels as described in a previous report (Montnach et al., 2022). Automated patch-clamp recordings in whole-cell configuration were performed using the SyncroPatch 384PE from Nanion (München, Germany). Chips with single-hole medium resistance of  $4.52 \pm 0.08 \text{ M}\Omega$  ( $N = 384$  experiments) were used for recordings. Pulse generation and data collection were performed with the PatchControl384 v1.5.2 software (Nanion) and the Biomek v1.0 interface (Beckman Coulter, Brea, CA, USA). The intracellular solution contained (in mM): 10 CsCl, 110 CsF, 10 NaCl, 10 EGTA and 10 HEPES (pH 7.2, osmolarity 280 mOsm). The extracellular solution contained (in mM): 140 NaCl, 4 KCl, 2  $\text{CaCl}_2$ , 1  $\text{MgCl}_2$ , 5 glucose and 10 HEPES (pH 7.4, osmolarity 298 mOsm). Voltage clamp experiments were performed at a holding potential of  $-100 \text{ mV}$  at room temperature ( $18\text{--}22^\circ\text{C}$ ) and currents were sampled at 20 kHz. Each peptide was prepared in the extracellular solution supplemented with 3% bovine serum albumin (BSA) and a single peptide concentration was applied to each cell. For establishing dose–response curves, the compounds were tested at a test potential of 0 mV for 50 ms with a pulse every 5 s. The percentage of current inhibition by the peptides was measured at equilibrium of blockage or at the end of a 14 min application period. Note that the peptide used in this study (hwtx) was different from the active toxin in the caged compound described in our previous publication (Montnach et al., 2022).

### Manual patch clamp tests in $\text{Na}_v1.2$ -expressing HEK293 cells

The HEK293-Nav1.2 cell line was transfected (using Eugene) by a BK-GFP channel cDNA (KCNMA1) inserted

in a pCMV6-AC plasmid. The BK channel-expressing cells were patched using an internal solution containing (in mM): 145 KCl, 2 NaCl, 10 HEPES, and 1 MgCl<sub>2</sub> (pH 7.2). The extracellular solution contained (in mM): 145 NaCl, 4 KCl, 1 MgCl<sub>2</sub>, 1 or 4 CaCl<sub>2</sub>, 5 HEPES and 5 glucose (pH 7.4).

### Brain slices solution, preparation and maintenance

The extracellular solution that we used contained (in mM): 125 NaCl, 26 NaHCO<sub>3</sub>, 1 MgSO<sub>4</sub>, 3 KCl, 1 NaH<sub>2</sub>PO<sub>4</sub>, 2 CaCl<sub>2</sub> and 20 glucose, bubbled with 95% O<sub>2</sub> and 5% CO<sub>2</sub>. Mice (C57BL/6j, 21–35 postnatal days old) purchased from Janvier Labs (Le Genest-Saint-Isle, France) were fed *ad libitum* until killing. Animals were anesthetized via isoflurane inhalation and the entire brain was removed after decapitation. Brain slices (350  $\mu$ m thick) were prepared using the procedure described in a previous report (Blömer et al., 2021), using a Leica VT1200 vibratome (Wetzlar, Germany). Slices were incubated at 37°C for 45 min and maintained at room temperature before use.

### Electrophysiology and imaging of brain slices

Slices with L5 pyramidal neurons in the somato-sensory cortex having an axon parallel to the slice surface were transferred to the recording chamber. Patch-clamp recordings were made at 32–34°C using a Multiclamp 700A (Molecular Devices, Sunnyvale, CA, USA). The intracellular solution contained (in mM): 125 KMeSO<sub>4</sub>, 5 KCl, 8 MgSO<sub>4</sub>, 5 Na<sub>2</sub>-ATP, 0.3 Tris-GTP, 12 Tris-phosphocreatine and 20 HEPES, adjusted to pH 7.35 with KOH. In Na<sup>+</sup> imaging experiments, the Na<sup>+</sup> indicator ING-2 (IonBiosciences, San Marcos, TX, USA) was added to the intracellular solution at a concentration of 0.5 mM and recordings were started 20 min after achieving the whole cell configuration. In V<sub>m</sub> imaging experiments, cell membranes were loaded with the voltage-sensitive dye D-2-ANEPEQ (JPW1114, 0.2 mg/mL, Thermo Fisher Scientific, Waltham, MA, USA) for 30 min using a first patch clamp recording and then re-patched a second time with dye-free solution. Finally, in Ca<sup>2+</sup> imaging experiments, the Ca<sup>2+</sup> indicator Oregon Green BAPTA-5N (OG5N; Thermo Fisher Scientific) was added to the intracellular solution at a concentration of 2 mM and recordings started 20 min after achieving the whole cell configuration. Somatic APs were elicited in current clamp mode by short current pulses of 1.5–2.5 nA through the patch pipette and electrical signals were acquired at 20 kHz. The bridge was corrected offline by using the recorded injected current and the measured V<sub>m</sub> was corrected for –11 mV junction potential. Na<sup>+</sup>

and Ca<sup>2+</sup> imaging experiments and most V<sub>m</sub> imaging experiments were performed using an imaging system described in previous reports (Filipis & Canepari, 2021; Filipis et al., 2018), based on an upright Scientifica SliceScope microscope equipped with a motorized XY translation stage and PatchStar manipulators (Scientifica, Uckfield, UK), and a 60 $\times$  Olympus water immersion objective (NA = 1). Na<sup>+</sup> and V<sub>m</sub> indicators were excited using the 520 nm line of a LaserBank (Cairn Research, Faversham, UK) band-pass filtered at 517  $\pm$  10 nm and directed to the preparation using a 538 nm long-pass dichroic mirror. The Ca<sup>2+</sup> indicator was excited using the 465 nm line of the LaserBank, band-pass filtered at 469  $\pm$  17 nm and directed to the preparation using a 495 nm long-pass dichroic mirror. Na<sup>+</sup> and V<sub>m</sub> fluorescence emission signals were band-pass filtered at 559  $\pm$  17 nm or long-pass filtered at >610 nm, respectively. Ca<sup>2+</sup> fluorescence emission was band-pass filtered at 525  $\pm$  25 nm. The size of the illumination spot, obtained using a custom-made telescope, was  $\sim$ 30  $\mu$ m. Image sequences were demagnified by 0.5 $\times$  and acquired with a DaVinci 2K CMOS camera (SciMeasure, Decatur, GA, USA) at 10 kHz with a pixel resolution of 500 nm in regions of 30  $\times$  128 pixels. The other V<sub>m</sub> imaging experiments were performed using an imaging system described in recent reports (Ait Ouares & Canepari, 2020; Ait Ouares et al., 2019). Fluorescence was excited using the 528 nm line of an LDI-7 laser (89 North, Williston, VT, USA), band-pass filtered at 531  $\pm$  40 nm and directed to the preparation using a 575 nm long-pass dichroic mirror. Fluorescence emission was long-pass filtered at >610 nm and acquired with a NeuroCCD camera (Redshirt Imaging, Decatur, GA, USA) at 20 kHz with a pixel resolution of  $\sim$ 2  $\mu$ m in regions of 4  $\times$  26 pixels. In all experiments, image sequences were acquired for 8 ms.

### Pharmacology

All molecules were initially dissolved in stock solutions and small aliquots were kept at –20°C before use. G<sup>1</sup>G<sup>4</sup>-huwentoxin-IV (hwtx) was synthesized by Smartox Biotechnology (Saint Egrève, France).  $\omega$ -Agatoxin-IVA (agaIVA),  $\omega$ -conotoxin-GVIA (conGVIA), snx482, apamin (apam) and iberitoxin (ibtx) were also purchased from Smartox Biotechnology. 4,9-Anhydrotetrodotoxin (attx) was purchased from Tocris (Bristol, UK). Tram-34 (tram) was purchased from HelloBio (Bristol, UK). All these molecules were initially dissolved in water at 100  $\mu$ M concentration and then diluted in external solution at the desired concentration. 4-(2,1,3-Benzoxadiazol-4-yl)–1,4-dihydro-2,6-dimethyl-3,5-pyridinecarboxylic acid methyl 1-methylethyl ester



(isradipine or isr) (HelloBio) was initially dissolved at 20 mM in DMSO and then diluted in external solution to 20  $\mu$ M just before use. This final solution was kept for a maximum of 1 h to prevent the loss of dissolved molecules due to precipitation. 3,5-Dichloro-*N*-[[[(1 $\alpha$ ,5 $\alpha$ ,6-*exo*,6 $\alpha$ )-3-(3,3-dimethylbutyl)-3-azabicyclo[3.1.0]hex-6-yl)methyl]-benzamide-hydrochloride (ML218 or ml) was purchased from Tocris and initially dissolved at 50 mM in DMSO. (1*S*,2*S*)-2-[2-[[3-(<sup>1</sup>H-benzimidazol-2-yl)propyl)methylamino]ethyl]-6-fluoro-1,2,3,4-tetrahydro-1-(1-methylethyl)-2-naphthalenyl-cyclopropanecarboxylate-dihydrochloride (NNC550396 or nnc) was purchased from Tocris and initially dissolved at 25 mM in water. These two molecules were diluted together in external solution at the desired concentrations. The protocol to locally deliver the channel blockers over the AIS is illustrated in Fig. 1*A*.

## Data analysis

All data, from averages of four trials with identical somatic response, were analysed using custom-written code written in MATLAB. Initially, recordings including an AP were corrected for photo-bleaching using multi-exponential fits of fluorescence transients in single trials without an AP. Then, the fractional change of fluorescence from the first image ( $\Delta F/F_0$ ) was calculated over the mean fluorescence in 5  $\mu$ m regions at proximal and distal locations of the AIS. Specifically, the protocol that we used in this study for ultrafast imaging from the AIS at 10 kHz is illustrated in Fig. 1*B*. Given the morphological variability, we standardized our analyses to regions of 5  $\mu$ m lengths within the proximal (prox) part of the AIS, at 5–15  $\mu$ m from soma, indicated by '1' in all figures, and to regions of 5  $\mu$ m lengths within distal (dist) parts of the AIS, at 30–40  $\mu$ m from soma, indicated by '2'

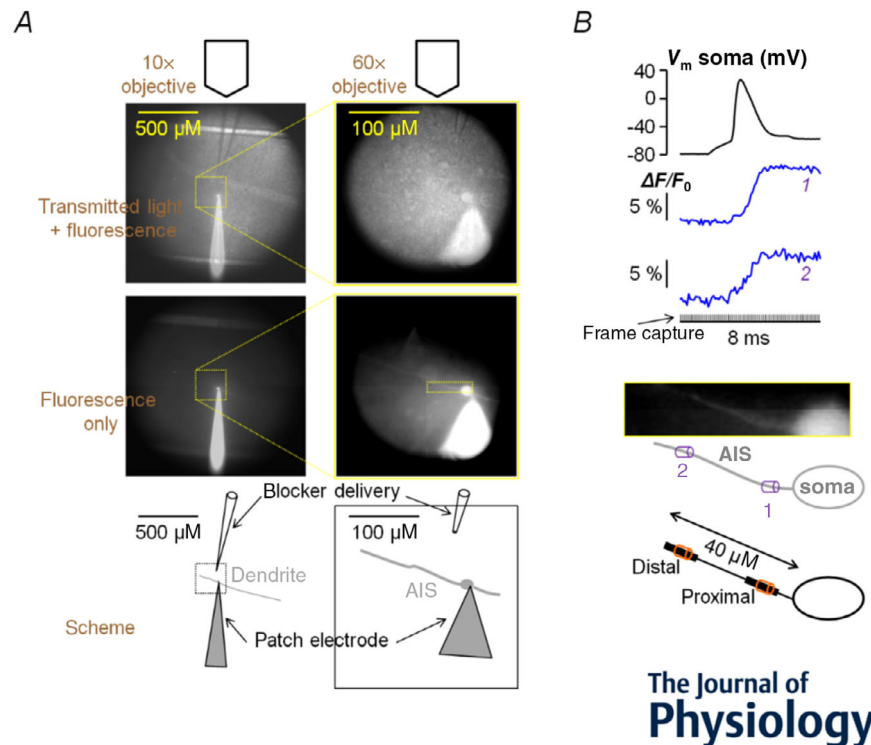


**Figure 1.** Illustrations of the experimental configuration and of the recording protocol used in the study *A*, illustration of the experimental configuration. Brain slice (somatosensory cortex) visualized by the DaVinci-2K camera using a 10 $\times$  magnification objective (images on the left) and a 60 $\times$  magnification objective (images on the right); the images on the top are taken with transmitted IR light and fluorescence simultaneously; the images below are taken with fluorescence only; as indicated below, a patch clamp electrode (also used to elicit APs and to record somatic  $V_m$ ) is used to load through the soma an L5 pyramidal neuron with a fluorescence indicator, while a pipette positioned near the AIS is used to locally deliver a solution containing a channel blocker, by gentle pressure application, for 1 min. *B*, in the recording protocol, images of  $\sim 64 \times 15 \mu\text{m}^2$  comprising the AIS are acquired at a frame rate of 10 kHz; to unambiguously distinguish signals from proximal and distal areas of the AIS, with respect to the soma, we systematically analysed every signal in a region 5  $\mu\text{m}$  long at position '1', within 5 and 15  $\mu\text{m}$  from the soma and in another region 5  $\mu\text{m}$  long at position '2', within 30 and 40  $\mu\text{m}$  from the soma; on the top, an AP is elicited and recorded at the soma (at 20 kHz) and the fluorescence signals ( $\text{Ca}^{2+}$  in this example) at positions 1 and 2 are reported. [Colour figure can be viewed at [wileyonlinelibrary.com](http://wileyonlinelibrary.com)]

in all the figures. For  $\text{Na}^+$  imaging experiments, the  $\text{Na}^+$  current was calculated as described in detail in Filipis & Canepari (2021). Specifically,  $\Delta F/F_0$  signals were initially converted into  $\Delta[\text{Na}^+]$  signals and then into an  $\text{Na}^+$  (or a positive charge) superficial density using an estimate of the diameter of the axon. The signal was fitted with a model function (see Filipis & Canepari, 2021) and the current surface density (or simply the current) was finally obtained by calculating the time derivative of this fit. For  $V_m$  imaging experiments, axonal APs were not calibrated as done for dendritic APs in pyramidal neurons, since this procedure is based on the high expression of glutamate receptors (Vogt et al., 2011). To unambiguously quantify a change in AP beyond the noise of the optical recording, we calculated the integral of the  $\Delta F/F_0$  signal over a time window of 2.4 ms comprising the AP. For  $\text{Ca}^{2+}$  imaging experiments, the  $\text{Ca}^{2+}$  current was calculated as described in detail in Jaafari & Canepari (2016). Specifically,  $\Delta F/F_0$  signals were fitted with a model function consisting of the product of four sigmoid functions and the current was obtained by calculating the time derivative of this fit.

## Statistics

The effect of a channel blocker on a specific signal was quantified by computing its percentage change following local delivery of the blocker with respect to the control condition. To assess the consistency of the effect, for each protocol and in at least seven cells we performed both a parametric paired  $t$  test and a non-parametric Wilcoxon ranked sign test (using the MATLAB 'signrank' function) comparing the values in control conditions and the values after local delivery of the channel blocker. As the ' $P$ ' values in both tests were consistently similar, we considered 0.01 obtained with the paired  $t$  test as the threshold to describe an effect as significant.

## NEURON model

The NEURON model, built from the starting model reported in Hallermann et al. (2012, adapted for the mouse) and already utilized in our previous article (Filipis & Canepari, 2021), was developed by replicating the results of the computer simulations with  $V_m$ ,  $\text{Na}^+$  and  $\text{Ca}^{2+}$  imaging results from three cells where the somatic AP had very similar shape. The AIS (40  $\mu\text{m}$  long) has a semi-conical shape with initial diameter of 4.22  $\mu\text{m}$  and final diameter of 1.73  $\mu\text{m}$  and it is divided in 20 compartments of 2  $\mu\text{m}$  length. We took the 6th compartment (10–12  $\mu\text{m}$  from the soma) as representative of the proximal AIS and the 16th compartment (30–32  $\mu\text{m}$  from the soma) as representative of the distal AIS. Construction of the

new model, from the initial basic model, was achieved through a strategy consisting of a sequence of steps.

- (1) First, we replaced the two generic VGNCs with the  $\text{Na}_v1.2$  and  $\text{Na}_v1.6$  channel models proposed in Mainen et al. (1995), also imposing the distribution of the initial model consistent with the results reported in Hu et al. (2009). The functions and distributions of both channels were then optimized to take into account the different activation and inactivation kinetics to match the experimental  $\text{Na}^+$  transients both in the proximal and in the distal parts of the AIS.
- (2) Second, we introduced  $\text{Ca}^{2+}$  permeability to  $\text{Na}_v1.2$  corresponding to 0.4% with respect to the permeability for  $\text{Na}^+$  (as suggested by Hanemaaijer et al., 2020), a low voltage-activated VGCC (LVAC), corresponding to T-type channels, and a high voltage-activated VGCC (HVAC), corresponding to the ensemble of L-type, P/Q-type, N-type and R-type channels. The two models were adopted from a model in Almog & Komgreen (2014). The channel distribution and density were set to match the results of the  $\text{Ca}^{2+}$  imaging experiment. The distribution of VGCCs was also consistent with the results reported by another laboratory (Lipkin et al., 2021). In the simulations used to match experimental  $\text{Ca}^{2+}$  transients, we introduced a generic mobile  $\text{Ca}^{2+}$  buffer with standard kinetics (Canepari & Mammano, 1999) to mimic 2 mM OG5N in the patch pipette. In all simulations, we accounted for an immobile endogenous buffer with capacity of  $\sim 40$  in the distal AIS, consistent with estimates at presynaptic sites (Delvendahl et al., 2015). Finally, for  $\text{Ca}^{2+}$  extrusion and  $\text{Ca}^{2+}$  radial/longitudinal diffusion, we used the model proposed in Kim et al. (2015).
- (3) Third, we modified the  $\text{K}^+$  channels from the initial model in the following manner. We introduced the inward rectifier  $\text{K}^+$  channels from Migliore et al. (2008), the BK CAKC from Ait Ouares et al. (2019) and the SK CAKC from Mahapatra et al. (2018), and we reduced the original  $\text{K}^+$  channels in order to preserve the kinetics of the AP in the AIS under control conditions. In addition, we explicitly made SK channel activation dependent on  $\text{Ca}^{2+}$  entering from LVACs. These modified profiles of  $\text{K}^+$  channels produced AP waveforms qualitatively consistent with  $V_m$  imaging experiments, when 80% of VGCCs, BK channels or SK channels were eliminated from the model.

With this model, we finally mimicked the delivery of 80 nM hwtx by changing the  $\text{Na}_v1.2$  function to obtain a reduction of the  $\text{Na}^+$  transients in the proximal and distal AIS consistent with the  $\text{Na}^+$  imaging experiments. This was done by full block of a non-inactivating component of the  $\text{Na}_v1.2$  current, 20% reduction of a fast inactivating

component of the  $\text{Na}_v1.2$  current, 6% reduction of the activation slope of the  $\text{Na}_v1.2$  current and 50% reduction of the  $\text{Ca}^{2+}$  permeability.

### Data and code availability

The complete dataset of imaging/electrophysiological experiments in brain slices, used in this study, is available in the public repository Zenodo (<https://zenodo.org/record/5835995>). The NEURON model, including the changes of parameters replicating the experiments with hwtx, are available in the NeuronDB database at: <http://modeldb.yale.edu/267355>. Matlab codes used for data analysis are available at <https://github.com/MarcoCanepari/NAV12-BK-paper>.

## Results

### Selectivity of hwtx for $\text{Na}_v1.2$ and of attx for $\text{Na}_v1.6$

The first necessary condition to unambiguously investigate the role of  $\text{Na}_v1.2$  in the AP generation at the AIS of L5 pyramidal neurons is the availability of a selective blocker of this channel that is specifically inert with respect to  $\text{Na}_v1.6$ . Phrixotoxin-3 (Bosmans et al., 2006) has been reported to be selective for  $\text{Na}_v1.2$ , but when we tested this peptide in L5 pyramidal neurons we found variable and rapidly reversible effects at the lowest concentrations where this selectivity is expected to apply. Thus, to produce a less reversible but still selective effect on  $\text{Na}_v1.2$  channels, we used a peptide modified from huwentoxin-IV (Xiao et al., 2011) where the two glutamate residues at positions 1 and 4 were replaced with two glycine residues. This peptide (hwtx) exhibits higher selectivity for  $\text{Na}_v1.2$  with respect to  $\text{Na}_v1.6$  at nanomolar concentrations as measured in HEK293 cells using automated patch-clamp recordings (Fig. 2A). Specifically, at 1 and 3.3 nM, hwtx blocks  $16 \pm 7$  and  $53 \pm 7\%$   $\text{Na}_v1.2$  currents respectively, and only  $5 \pm 4$  and  $9 \pm 5\%$   $\text{Na}_v1.6$  currents respectively. The challenge remained to exploit this selectivity by locally blocking  $\text{Na}_v1.2$  in the AIS of L5 pyramidal neurons in the context of brain slices in which effective concentrations may differ. Thus, L5 pyramidal neurons were patched in the cell body, and another pipette near the AIS was used to locally deliver selective channel blockers, for 1 min, by gentle pressure application. In this way, when we delivered hwtx at 40 nM, the peptide did not affect the AP (Fig. 2A). The lower concentration at which we consistently observed an effect was 80 nM and this effect was a delay in the AP onset and peak with occasionally a small decrease in amplitude (Fig. 2A). Finally, at 160 nM, hwtx consistently produced a longer delay and decreased the amplitude of the AP. Importantly for this project, at all concentrations, the consistent effects of hwtx were stable for several minutes

after delivery, in sharp contrast to the case of phrixotoxin application. We could therefore use hwtx at 80 nM on the hypothesis that at this minimal concentration the peptide should produce a partial but selective block on  $\text{Na}_v1.2$  because this channel type is more sensitive than  $\text{Na}_v1.6$  to hwtx block. To validate whether any finding obtained by local delivery of hwtx was exclusively due to  $\text{Na}_v1.2$ , we used in assessment experiments the  $\text{Na}_v1.6$  inhibitor attx. We assessed, in experiments performed in HEK293 cells using automated patch clamp recordings (Fig. 2B), that this molecule exhibits a moderate selectivity for  $\text{Na}_v1.6$  with respect to  $\text{Na}_v1.2$ . Specifically, at 10 and 33 nM, attx blocks  $20 \pm 13$  and  $30 \pm 13\%$   $\text{Na}_v1.6$ , respectively, whereas it blocks  $9 \pm 11\%$  and  $16 \pm 12\%$   $\text{Na}_v1.2$  respectively. In AP tests performed in brain slices, attx at 400 nM did not affect the AP, whereas the lowest concentration at which we consistently observed a delay in the AP offset was 800 nM (Fig. 2B). At 1600 nM, attx consistently produced a stronger AP inhibition (Fig. 2B). Similarly to hwtx, the effects of attx at all concentrations were stable for several minutes after delivery. Thus, assessment experiments were performed by using attx at the concentration of 800 nM that provides the minimal perturbation of the somatic AP.

### Selective block of $\text{Na}_v1.2$ reduces the $\text{Na}^+$ current associated with the AP waveform in the AIS

To investigate how the partial block of  $\text{Na}_v1.2$  effects the signals associated with the generating AP in the AIS, we started by analysing the  $\text{Na}^+$  currents measured optically as described in Filipis & Canepari (2021). Fig. 3A shows the AIS of a neuron filled with the  $\text{Na}^+$  indicator Ion Natrium Green-2 (ING-2). We first measured the sodium concentration change ( $\Delta[\text{Na}^+]$ ) associated with an AP and then we calculated the  $\text{Na}^+$  current ( $I_{\text{Na}}$ ) as the time-derivative of the fit of the  $\Delta[\text{Na}^+]$  signal using a model function (Fig. 3B). In the example of Fig. 3A, application of 80 nM hwtx produced a decrease of  $\sim 30\%$  of the  $\Delta[\text{Na}^+]$  signal in the proximal part of the AIS and an  $\sim 15\%$  decrease in the distal part. As already reported (Filipis & Canepari, 2021), the  $I_{\text{Na}}$  is characterized by a fast inactivating component ( $I_{\text{fast}}$ ) and a slow non-inactivating component ( $I_{\text{slow}}$ ). Thus, we systematically evaluated the change in the  $I_{\text{fast}}$  peak and in the  $I_{\text{slow}}$  (defined as the mean  $I_{\text{Na}}$  in the 1 ms following the AP peak) after hwtx. On average, in nine cells analysed, we found a significant decrease in the  $\Delta[\text{Na}^+]$  ( $P = 0.0023$ , paired  $t$  test) and in the  $I_{\text{fast}}$  signals ( $P = 0.0025$ , paired  $t$  test), both in proximal and distal regions, whereas a consistent but more variable decrease in the  $I_{\text{slow}}$  signals was estimated. In proximal regions, where  $\text{Na}_v1.2$  is expected to be dominant, the decrease in  $\Delta[\text{Na}^+]$  and  $I_{\text{fast}}$  signals were 30 and 36% respectively, indicating a block of 30–40% of



Na<sup>+</sup> channels (Fig. 3C). According to the selectivity curve reported in Fig. 2A, this percentage block is within the range where hwtx is inert to Na<sub>v</sub>1.6.

### Selective block of Na<sub>v</sub>1.2 widens the generating AP waveform in the AIS

The important finding that local delivery of 80 nM hwtx blocks 30–40% of Na<sub>v</sub>1.2 without affecting Na<sub>v</sub>1.6 allowed us to perform further experiments with high confidence using hwtx at 80 nM. It permitted analysis of the axonal AP waveform change after reducing Na<sub>v</sub>1.2, using *V<sub>m</sub>* imaging with the voltage-sensitive dye JPW1114. In the example of Fig. 4A, application of 80 nM hwtx delayed the onset of the AP, consistently with what we reported in Figs 2A and 3. In the distal AIS, however, it also changed

the shape of the AP by widening its waveform (Fig. 4B). To reliably quantify the waveform change beyond the noise limitations, we calculated the time integral of the *V<sub>m</sub>* signal in control conditions and after hwtx application over a time-window of 2.4 ms containing the AP (*∫V<sub>m</sub>*). Notably, in nine cells analysed, the *∫V<sub>m</sub>* at its last value increased significantly by  $21.3 \pm 10.5\%$  ( $P = 0.00024$ , paired *t* test) in the distal regions of the AIS (Fig. 4C). This result indicates that Na<sub>v</sub>1.2 is contributing to shaping of the generating AP and that these channels are activated by Ca<sup>2+</sup> influx via Na<sub>v</sub>1.2. Since Na<sub>v</sub>1.2 is also permeable to Ca<sup>2+</sup> and it was reported that Na<sub>v</sub>1.2 mediates Ca<sup>2+</sup> influx in the AIS during APs (Hanemaaijer et al., 2020), we next investigated this phenomenon in detail using hwtx.

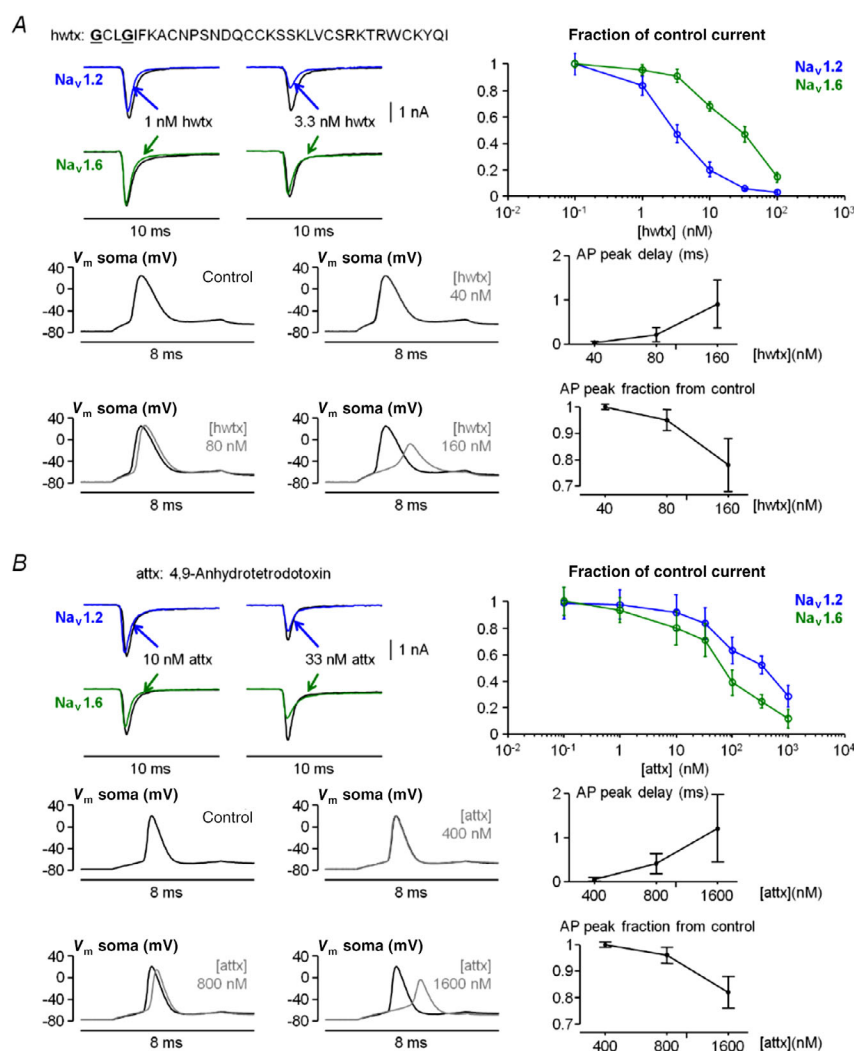


**Figure 2. Selectivity of <sup>1</sup>G<sup>4</sup>Huwentoxin-IV (hwtx) and of 4,9-Anhydrotetrodotoxin (attx)**

A, top-left, currents in HEK293 cells expressing either Na<sub>v</sub>1.2 (blue) or Na<sub>v</sub>1.6 (green) in control solution and after addition of hwtx at 1 nM (left traces) or at 3.3 nM (right traces); the 35 amino acid sequence of hwtx is reported; the two residues mutated from the wild-type peptide are indicated with bold-underlined characters. Top-right, fraction of Na<sub>v</sub>1.2 (green) or Na<sub>v</sub>1.6 (blue) current peak from control condition (no hwtx) against hwtx concentration (mean  $\pm$  SD); each concentration-point has been calculated over 10–15 cells. Bottom-left, in an L5 pyramidal neuron in brain slices, AP elicited under control conditions (no hwtx) or in the presence of 40, 80 or 160 nM hwtx. Bottom-right, delay of the AP peak and AP peak fraction from the control condition against hwtx concentration (mean  $\pm$  SD,  $N = 7$  cells). B, top-left, currents in HEK293 cells in control solution and after addition of attx at 10 nM (left traces) or at 33 nM (right traces). Top-right, fraction of Na<sub>v</sub>1.2 or Na<sub>v</sub>1.6 current peak from control condition (no attx) against attx concentration (mean  $\pm$  SD); each concentration-point has been calculated over 10–15 cells. Bottom-left, in an L5 pyramidal neuron in brain slices, AP elicited under control conditions (no attx) or in the presence of 400, 800 or 1600 nM attx. Bottom-right, delay of the AP peak and AP peak fraction from the control condition against attx concentration (mean  $\pm$  SD,  $N = 7$  cells). [Colour figure can be viewed at [wileyonlinelibrary.com](http://wileyonlinelibrary.com)]

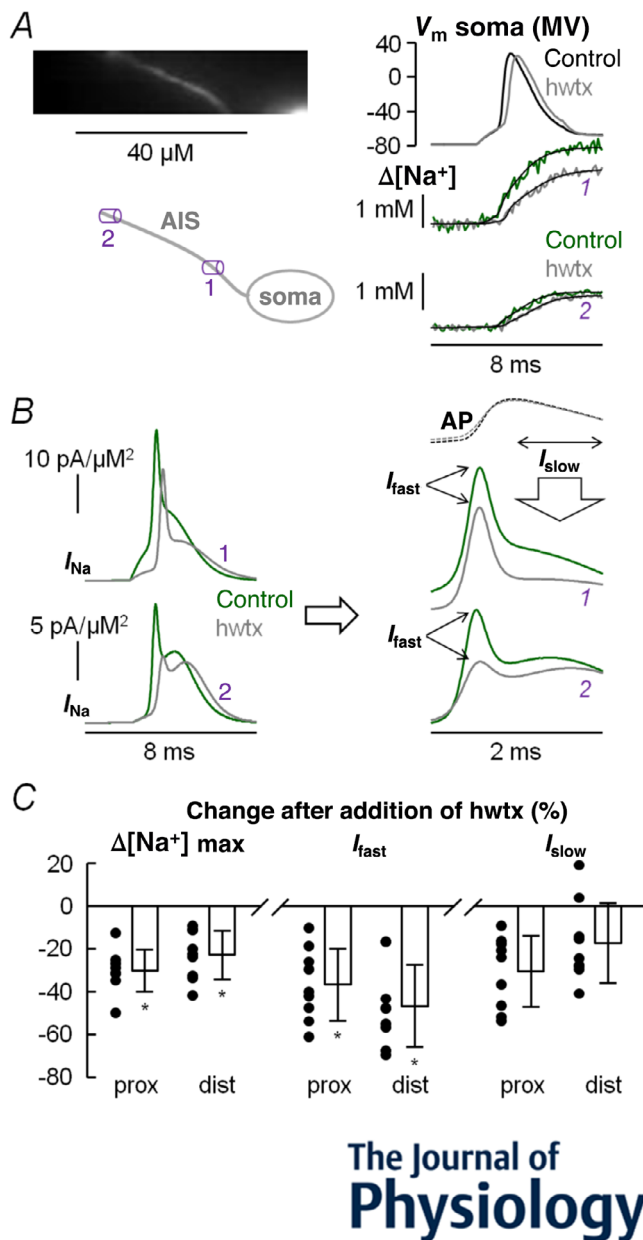


**Figure 3.** Effect of hwtx (block of  $\text{Na}_v1.2$ ) on the  $\text{Na}^+$  influx in the AIS

A, left, fluorescence image ( $\text{Na}^+$  indicator ING-2) of the AIS and its reconstruction with a proximal region (1) and a distal region (2) indicated. Right, somatic AP in control solution and after local delivery of 80 nM hwtx (top) and associated corrected  $\text{Na}^+$  transients fitted with a model function in 1 and 2. B, left, from the experiment in A,  $\text{Na}^+$  currents calculated from the time-derivative of the  $\text{Na}^+$  transient fits. Right, zoom of the  $\text{Na}^+$  currents 1 ms before and 1 ms after the AP peak, indicating the fast component of the  $\text{Na}^+$  current ( $I_{\text{fast}}$ ) and the slow component of the  $\text{Na}^+$  current ( $I_{\text{slow}}$ ) defined as the mean  $\text{Na}^+$  current during the 1 ms interval after the AP peak. C, left, single cell values and percentage change ( $N = 9$  cells) of the  $\text{Na}^+$  transient maximum after locally delivering hwtx in proximal regions (mean  $\pm$  SD =  $-30.3 \pm 9.8$ ), and in distal regions (mean  $\pm$  SD =  $-22.9 \pm 11.4$ ). Centre, single cell values and percentage change of  $I_{\text{fast}}$  after locally delivering hwtx in proximal regions (mean  $\pm$  SD =  $-36.6 \pm 16.7$ ), and in distal regions

(mean  $\pm$  SD =  $-46.8 \pm 19.2$ ). Right, single cell values and percentage change of  $I_{\text{slow}}$  after addition of hwtx in proximal regions (mean  $\pm$  SD =  $-30.7 \pm 16.6$ ), and in distal regions (mean  $\pm$  SD =  $-17.5 \pm 18.6$ ). An asterisk indicates a significant change ( $*P < 0.01$ , paired  $t$  test). [Colour figure can be viewed at [wileyonlinelibrary.com](http://wileyonlinelibrary.com)]

### $\text{Na}_v1.2$ mediates $\text{Ca}^{2+}$ influx associated with the AP in the AIS

To investigate  $\text{Ca}^{2+}$  influx and currents associated with an AP in the AIS, we recorded  $\text{Ca}^{2+}$  fluorescence from the indicator OG5N and estimated the  $\text{Ca}^{2+}$  current waveform by calculating the time derivative of the fluorescence transient (Jaafari et al., 2014). Specifically, we fitted the fluorescence transient with a four-sigmoid fit and calculated its time-derivative as done in Jaafari & Canepari (2016). Since diverse types of VGCCs are expressed in the AIS of L5 pyramidal neurons (Lipkin et al., 2021), we preliminarily assessed the effects of inhibiting individual types of VGCCs. In detail, we blocked L-type VGCCs with 20  $\mu\text{M}$  isradipine, P/Q-type VGCCs with 1  $\mu\text{M}$   $\omega$ -agatoxin-IVA, N-type VGCCs with 1  $\mu\text{M}$   $\omega$ -conotoxin-GVIA, R-type VGCCs with 1  $\mu\text{M}$  SNX482, and T-type VGCCs with 5  $\mu\text{M}$  ML218 and 30  $\mu\text{M}$  NNC550396. The results of this accurate analysis, reported in Fig. 5, indicate that all types of VGCCs, at different extent, contribute to the axonal  $\text{Ca}^{2+}$  influx and current associated with the AP. Next, we analysed the kinetics of the  $\text{Ca}^{2+}$  current at different locations of the AIS as shown in the example of Fig. 6A. As already reported by Hanemaaijer et al. (2020), the kinetics of the  $\text{Ca}^{2+}$  signal associated with the AP varied with distance from the soma, with the onset of the  $\text{Ca}^{2+}$  transient in the distal axon preceding that in the proximal axon. In terms of  $\text{Ca}^{2+}$  currents calculated as time-derivatives of the  $\text{Ca}^{2+}$  transients, a substantial delay between the peak of the  $\text{Ca}^{2+}$  current in the distal axon and the peak of the  $\text{Ca}^{2+}$  in the proximal part of the AIS was measured (Fig. 6B). This behaviour was consistently observed in  $N = 61$  cells tested in this way (Fig. 6B), with delay between the peaks of the distal and the proximal  $\text{Ca}^{2+}$  currents of  $402 \pm 177 \mu\text{s}$ . The evident anticipation of the AP peak, also with respect to the somatic AP peak, suggests that the  $\text{Ca}^{2+}$  influx associated with the AP is mainly mediated by VGNCs in the distal axon, whereas it is mainly mediated by VGCCs in the proximal axon. To address this hypothesis, we assessed the effect of locally delivering 80 nM hwtx on the  $\text{Ca}^{2+}$  influx and current associated with the AP in the AIS. In the example of Fig. 6C, hwtx substantially decreased the distal  $\text{Ca}^{2+}$  influx and current associated with the AP, whereas it only slightly decreased the proximal  $\text{Ca}^{2+}$  influx. Since all VGCCs contribute to the  $\text{Ca}^{2+}$  signal, to assess the effect

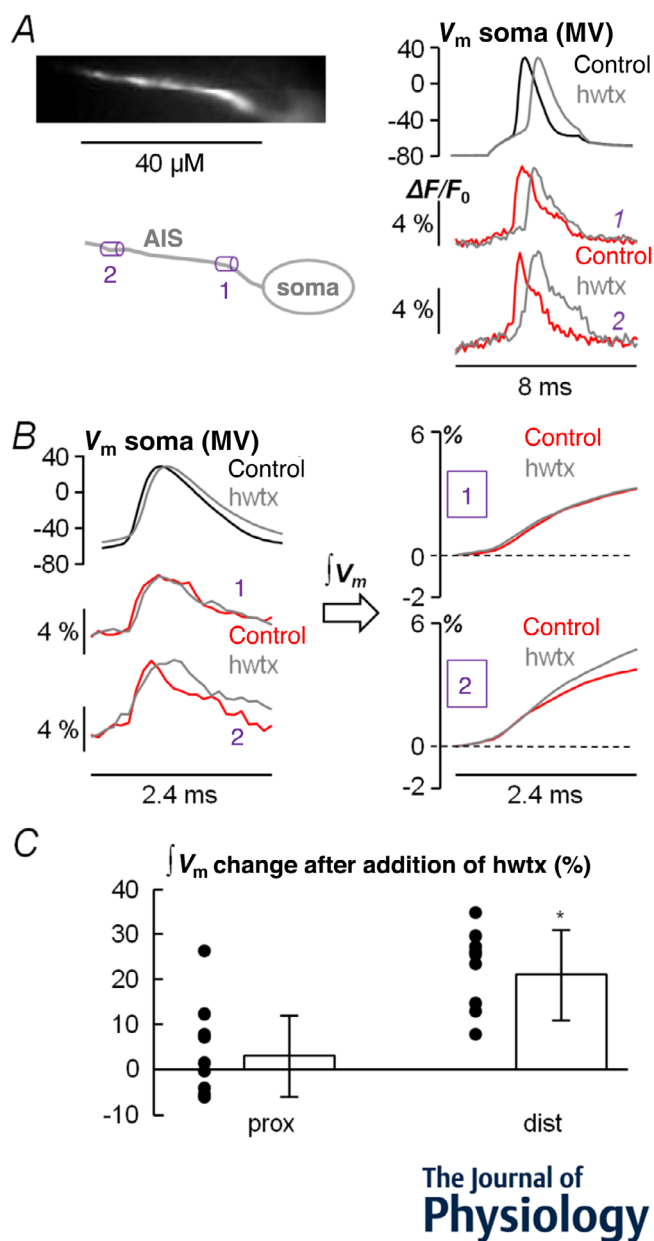


**Figure 4. Effect of hwtx (block of  $\text{Na}_v1.2$ ) on the AP waveform in the AIS**

A, left, fluorescence image (voltage-sensitive dye JPW1114) of the AIS and its reconstruction with a proximal region (1) and a distal region (2) indicated. Right, somatic AP in control solution and after locally delivering 80 nM of hwtx (top) and associated  $V_m$  transients in 1 and 2. B, left, somatic and axonal APs at a different time scale (2.4 ms duration) visually indicating a widening of the AP waveform, in the distal position only, after locally delivering hwtx. Right, quantification of the AP waveform shape by calculation of the  $V_m$  integral ( $\int V_m$ ) over the 2.4 ms time window comprising the AP signal. C, single cell values and percentage change ( $N = 9$  cells) of the  $\int V_m$  signal maximum after locally delivering hwtx in proximal regions (mean  $\pm$  SD =  $3.2 \pm 8.8$ ), and in distal regions (mean  $\pm$  SD =  $21.3 \pm 10.5$ ). An asterisk indicates a significant change ( $*P < 0.01$ , paired  $t$  test). [Colour figure can be viewed at [wileyonlinelibrary.com](http://wileyonlinelibrary.com)]

of blocking VGCCs we locally delivered a cocktail with all inhibitors of the tests reported in Fig. 5 at the same concentrations. In the example of Fig. 6D, the block of VGCCs substantially decreased the proximal  $\text{Ca}^{2+}$  influx and current associated with the AP, whereas the decrease of the distal  $\text{Ca}^{2+}$  current was only comparable to that produced by local delivery of 80 nM hwtx. We then compared the change of the  $\text{Ca}^{2+}$  current peak in  $N = 8$  cells where the effect of locally delivering the cocktail of VGCC blockers was tested (Fig. 6E). Whereas the partial block of  $\text{Na}_v1.2$  produced a marginal decrease of  $\sim 10\%$  of the  $\text{Ca}^{2+}$  current in the proximal AIS, compared to the significant decrease of  $>60\%$  produced by blocking VGCCs ( $P = 6.7 \times 10^{-5}$ , paired  $t$  test), in the distal AIS hwtx and VGCC blockers produced a similar and significant decrease of the  $\text{Ca}^{2+}$  current ( $P = 0.0048$  and  $P = 0.0024$ , paired  $t$  test). In summary, the results reported in Fig. 6E suggest that a substantial contribution of  $\text{Ca}^{2+}$  influx associated with the AP, at distal sites of the AIS, is mediated by  $\text{Na}_v1.2$ . Partial block of  $\text{Na}_v1.2$  can therefore reduce the  $\text{K}^+$  current mediated by CAKCs, widening the AP waveform at distal sites (Fig. 4).

#### Block of BK CAKCs widens the AP in the AIS preventing the widening caused by blocking $\text{Na}_v1.2$

In keeping with the results reported in Fig. 6, we next assessed the regulation of the AP waveform by individual CAKCs. In the example of Fig. 7A, locally delivering  $1 \mu\text{M}$  of the SK CAKC inhibitor apamin widened the AP waveform in the soma and in the proximal and distal sites of the AIS. Visually, this widening was larger towards the late phase of the repolarization. Similarly, in the example of Fig. 7B, locally delivering  $1 \mu\text{M}$  of the BK CAKC inhibitor iberiotoxin also widened the somatic and axonal AP waveforms, but in this case the widening was observed earlier during the repolarization. The widening behaviours produced by apamin or iberiotoxin were consistently observed in all cells tested. In contrast, the effects produced by blocking IK CAKCs expressed in L5 pyramidal neurons (Roshchin et al., 2020), using  $1 \mu\text{M}$  tram-34, were not significant. In the example of Fig. 7C, locally delivering tram-34 did not change the AP waveforms in the soma and at all sites of the AIS. In agreement with this initial analysis of CAKCs, we conducted a further analysis on SK and BK CAKCs only. To see whether a  $\text{Ca}^{2+}$  source activates a particular CAKC, one can block only this particular  $\text{Ca}^{2+}$  source and see whether this block prevents the effects produced by CAKCs. Thus, we first tested the combination of VGCCs as  $\text{Ca}^{2+}$  source by using the cocktail of blockers already used in the experiments of Fig. 6. In the example of Fig. 8A, we first blocked VGCCs,

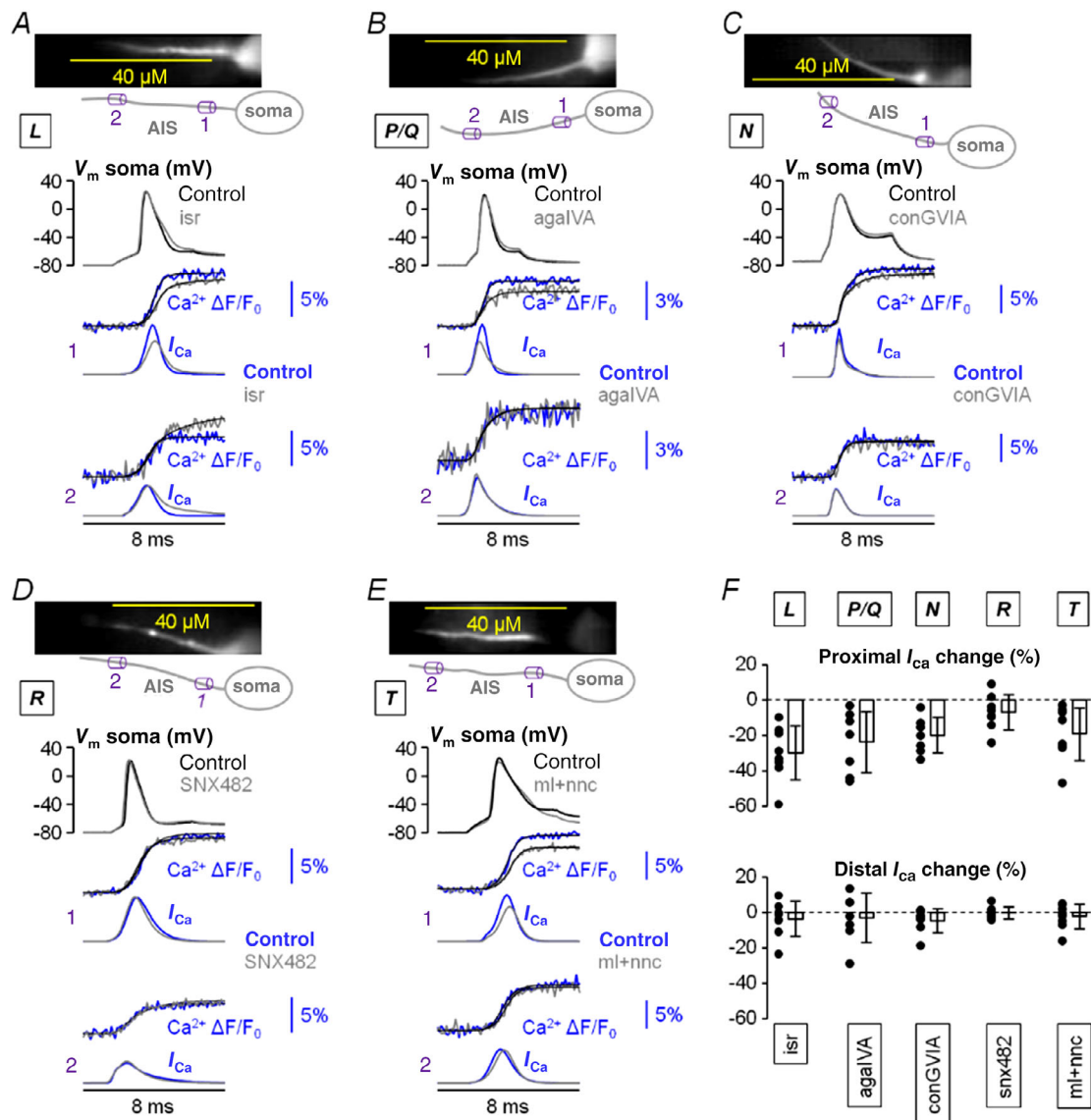
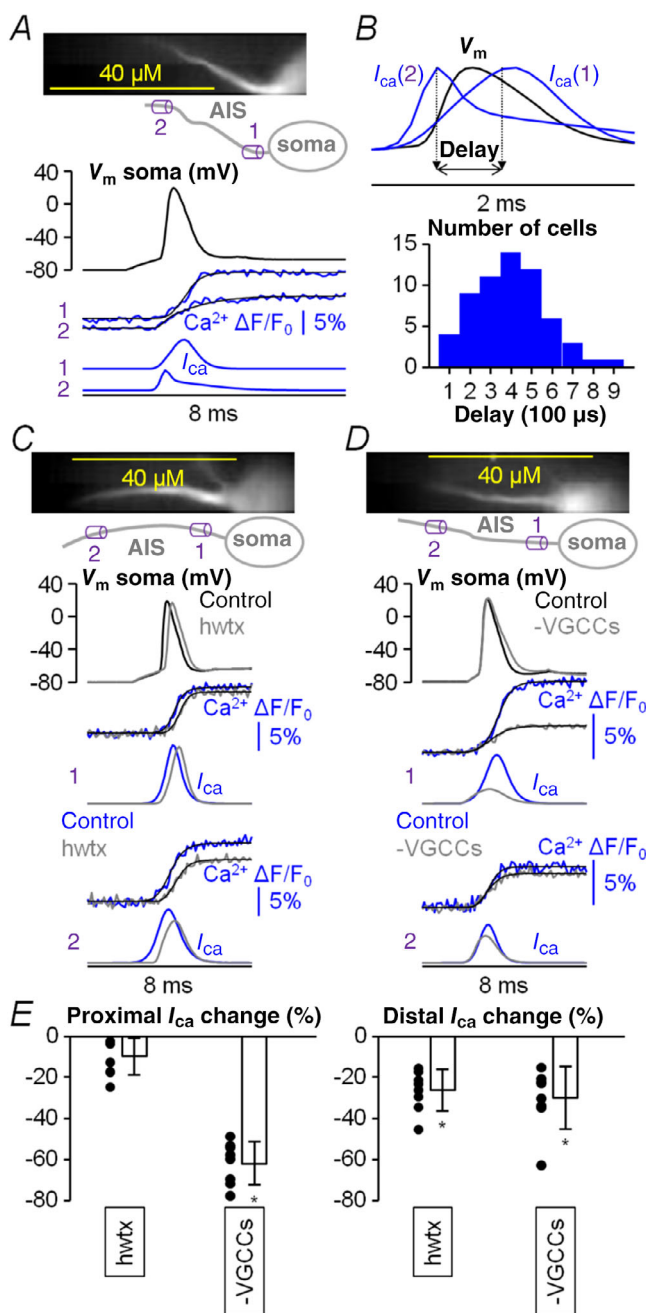


**Figure 5.** Analysis of the  $\text{Ca}^{2+}$  current ( $I_{\text{Ca}}$ ) components mediated by individual VGCC types in the AIS. A, top, fluorescence image ( $\text{Ca}^{2+}$  indicator OG5N) of the AIS and its reconstruction with a proximal region (1) and a distal (2) region indicated. Middle, somatic AP in control solution and after locally delivering 20  $\mu\text{M}$  of the L-type VGCC inhibitor isradipine (isr). Bottom,  $\text{Ca}^{2+}$  transients associated with the APs above fitted with the product of four sigmoid functions (black traces) and  $I_{\text{Ca}}$  signals derived from the fits. B, same protocol as in A, but locally delivering 1  $\mu\text{M}$  of the P/Q-type VGCC inhibitor  $\omega$ -agatoxin-IVA (agaIVA). C, same protocol as in A, but locally delivering 1  $\mu\text{M}$  of the N-type VGCC inhibitor  $\omega$ -conotoxin-GVIA (conGVIA). D, same protocol in A, but locally delivering 1  $\mu\text{M}$  of the R-type VGCC inhibitor SNX482. E, same protocol as in A, but locally delivering 5 and 30  $\mu\text{M}$ , respectively, of the T-type VGCC inhibitors ML218 and NNC550396 (ml+nnc). F, top, single values and percentage change of the  $I_{\text{Ca}}$  peak in proximal regions after addition of isr ( $N = 7$  cells, mean  $\pm$  SD =  $-29.9 \pm 17.0$ ), after addition of agaIVA ( $N = 8$  cells, mean  $\pm$  SD =  $-23.9 \pm 17.4$ ), after addition of conGVIA ( $N = 7$  cells, mean  $\pm$  SD =  $-20.2 \pm 10.1$ ), after addition of SNX482 ( $N = 8$  cells, mean  $\pm$  SD =  $-7.1 \pm 10.0$ ) or after addition of ml+nnc ( $N = 8$  cells, mean  $\pm$  SD =  $-19.0 \pm 14.9$ ). Bottom, in the same cells, single values and percentage change of the  $I_{\text{Ca}}$  peak in distal regions after addition of isr (mean  $\pm$  SD =  $-3.8 \pm 10.0$ ), after addition of agaIVA (mean  $\pm$  SD =  $-3.3 \pm 13.9$ ), after addition of conGVIA (mean  $\pm$  SD =  $-4.8 \pm 6.8$ ), after addition of SNX482 (mean  $\pm$  SD =  $-0.2 \pm 3.4$ ) or after addition of ml+nnc (mean  $\pm$  SD =  $-2.3 \pm 7.0$ ). [Colour figure can be viewed at [wileyonlinelibrary.com](http://wileyonlinelibrary.com)]

The Journal of  
Physiology





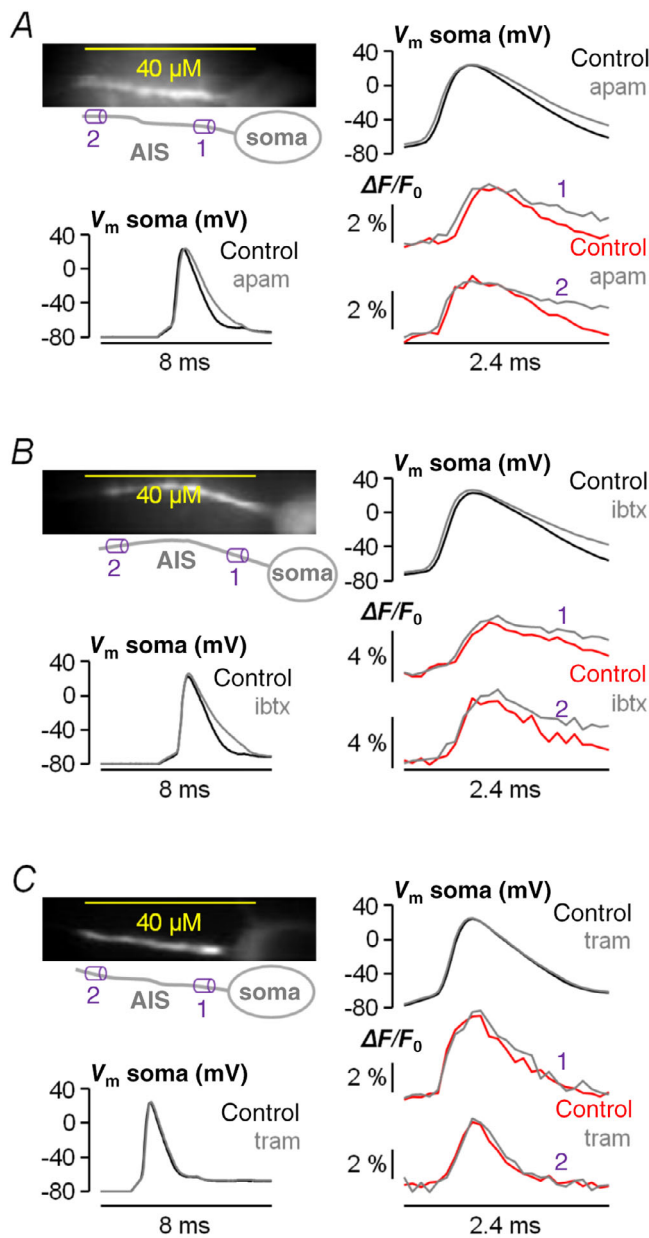
The Journal of  
Physiology

**Figure 6. Effect of hwtx (block of Nav1.2) on the  $Ca^{2+}$  influx in the AIS**

**A**, top, fluorescence image ( $Ca^{2+}$  indicator OG5N) of the AIS and its reconstruction with a proximal region (1) and a distal region (2) indicated. Bottom, somatic AP and associated  $Ca^{2+}$  transients fitted with a four-sigmoid (product of four sigmoids) function in 1 and 2; the  $Ca^{2+}$  currents calculated as the time-derivative of the fits are reported below. **B**, top, from the experiment in **A**,  $Ca^{2+}$  currents superimposed on the somatic AP. Bottom, over  $N = 61$  cells tested, the distribution of the delay between the distal and the proximal  $Ca^{2+}$  current peaks. **C**, top,  $Ca^{2+}$  fluorescence image of the AIS and

its reconstruction with a proximal region (1) and a distal (2) region indicated. Bottom, somatic AP and associated  $Ca^{2+}$  transients and currents in control solution and after local delivery of 80 nM hwtx (top) at 1 and 2. **D**, in another cell, same protocol as that reported in **C**, but with local delivery of a cocktail blocking all VGCCs (-VGCCs) comprising 20  $\mu$ M isradipine (L-type), 1  $\mu$ M  $\omega$ -agatoxin-IVA (P/Q-type), 1  $\mu$ M  $\omega$ -conotoxin-GVIA (N-type), 1  $\mu$ M SNX482 (R-type) or 5  $\mu$ M ML218 + 30  $\mu$ M NNC550396 (T-type). **E**, left, single values and percentage change of the proximal  $Ca^{2+}$  current peak after addition of hwtx ( $N = 8$  cells, mean  $\pm$  SD =  $-9.7 \pm 8.9$ ) or after addition of VGCCs blockers ( $N = 8$  cells, mean  $\pm$  SD =  $-62.2 \pm 10.5$ ). Right, in the same cells, single values and percentage change of the distal  $Ca^{2+}$  current peak after addition of hwtx (mean  $\pm$  SD =  $-26.2 \pm 10.1$ ) or after addition of VGCCs blockers (mean  $\pm$  SD =  $-30.0 \pm 15.1$ ). An asterisk indicates a significant change (\* $P < 0.01$ , paired  $t$  test). [Colour figure can be viewed at [wileyonlinelibrary.com](http://wileyonlinelibrary.com)]

observing a widening of the AP waveform in the soma and in the proximal and distal sites of the AIS, and then added apamin to the cocktail of VGCC blockers. Block of SK CAKCs did not further change the somatic and axonal AP waveforms once VGCCs were blocked. In contrast, in the example of Fig. 8B, after observing a widening of the somatic and axonal AP waveforms produced by blocking VGCCs, addition of iberitoxin caused a further widening of the  $V_m$  signals. Quantitative assessment of the effects of apamin and iberitoxin was done in four separate groups of seven cells in which the two inhibitors were tested first in control conditions and then after blocking VGCCs. In control conditions, the delivery of SK CAKC, BK CAKC or VGCC inhibitors, but not the delivery of the IK CAKC inhibitor, produced a significant increase of the  $fV_m$  signal (Fig. 8C) both in the proximal ( $P = 0.0042$ ,  $P = 0.0063$  and  $P = 0.00064$ , paired  $t$  test) and in the distal ( $P = 0.0079$ ,  $P = 0.0011$  and  $P = 0.00042$ , paired  $t$  test) sites of the AIS. Visually, this effect was larger at distal sites of the AIS for the BK CAKC inhibitor whereas the widening effects produced by apamin were similar to those produced by blocking VGCCs ( $N = 14$  cells). When VGCCs were previously blocked, further addition of apamin did not change the  $fV_m$  signal (Fig. 8D). In contrast, further addition of iberitoxin increased the  $fV_m$  signal, in a significant manner, by  $\sim 12\%$  at the proximal AIS sites ( $P = 0.0065$ , paired  $t$  test) and by  $\sim 21\%$  at the distal AIS sites ( $P = 0.0039$ , paired  $t$  test) (Fig. 8D). We concluded that SK CAKCs are activated exclusively by VGCCs, whereas BK CAKCs are also activated by other  $Ca^{2+}$  sources. Thus, to finally establish whether BK CAKCs are the target of  $Ca^{2+}$  entering through  $Na_v1.2$ , we measured the change in the AP waveform produced by locally delivering 80 nM hwtx, in the presence of 1  $\mu$ M iberitoxin. In contrast to the cell shown in Fig. 4A and B where hwtx was applied in control solution, in the cell shown in Fig. 9A hwtx local delivery still slightly shifted the AP onset, but it did not change the  $fV_m$



The Journal of  
Physiology

**Figure 7. Effect of blocking SK CAKCs, BK CAKCs or IK CAKCs on the AP waveform in the AIS**

A, left, fluorescence image (JPW1114) of the AIS and its reconstruction with a proximal region (1) and a distal (2) region indicated; somatic AP before and after locally delivering 1  $\mu$ M of the SK CAKC inhibitor apamin (apam) reported below. Right, somatic AP in control solution and after apamin delivery and associated  $V_m$  transients in 1 and 2. B, in another cell, same protocol as in A but by locally delivering 1  $\mu$ M of the BK CAKC inhibitor iberiotoxin (ibtX). C, in another cell, same protocol as in A but by locally delivering 1  $\mu$ M of the IK CAKC inhibitor tram-34 (tram). [Colour figure can be viewed at [wileyonlinelibrary.com](http://wileyonlinelibrary.com)]

signals. In this final quantitative assessment performed in a group of seven cells (Fig. 9B), addition of hwtX in the presence of iberiotoxin did not change the  $\int V_m$  signal, in contrast to the increase of the  $\int V_m$  signal observed without iberiotoxin. This result indicates that the block of BK CAKCs prevents further widening of the AP waveform, in the AIS, produced by the block of  $\text{Na}_v1.2$ . We concluded that the  $\text{Na}_v1.2$   $\text{Ca}^{2+}$  influx targets BK CAKCs, in this way shaping the AP waveform at its generating site.

### **$\text{Na}_v1.6$ does not mediate $\text{Ca}^{2+}$ influx associated with the AP in the AIS**

The experiments reported in Figs. 3–9 demonstrate that  $\text{Na}_v1.2$  in the AIS shapes the AP waveform during the rising phase, by providing a large fraction of the inward current, and in the falling phase by regulating the  $\text{Ca}^{2+}$ -activated outward current. The other VGNC ( $\text{Na}_v1.6$ ) also contributes to AP shaping by providing the other  $\text{Na}^+$  inward current, but whether it also regulates the  $\text{Ca}^{2+}$ -activated outward current remained to be established. In a final set of experiments, we addressed this question by performing the same tests we did with hwtX (Figs. 3, 4 and 6), but in this case using the  $\text{Na}_v1.6$  inhibitor attX at 800 nM (see Fig. 2B). Surprisingly, in the cell reported in Fig. 10A, local attX delivery produced an increase of the distal  $\text{Na}^+$  transient, associated with a large increase of the slow non-inactivating component of the  $\text{Na}^+$  current (Fig. 10B). A large increase of the  $\text{Na}^+$  transient and of the  $I_{\text{slow}}$  at distal sites was observed in 4/8 cells tested with this protocol (Fig. 10C), suggesting that attX slows down the kinetics of inactivation of VGNCs. Consistently with a variable modulation of the  $I_{\text{slow}}$ , attX also produced inconsistent effects on the axonal AP waveform. While in the cell reported in Fig. 11A and B the local delivery of attX did not change the AP waveform in the AIS, in the cell reported in Fig. 11C and D attX widened the AP at the distal site of the AIS. In  $N = 7$  cells tested with this protocol, the widening of the distal axonal AP was not statistically significant (Fig. 11E). The complex interaction of attX with VGNCs does not allow the use of this tool to analyse in detail the role of  $\text{Na}_v1.6$ . Nevertheless, because attX prolongs the  $\text{Na}^+$  influx (Fig. 10A), the  $\text{Ca}^{2+}$  influx should be also prolonged if the channel affected by attX is permeable to  $\text{Ca}^{2+}$ . In the cell of Fig. 12A, however, local delivery of attX did not change the axonal  $\text{Ca}^{2+}$  current and no significant change of the proximal or distal axonal  $\text{Ca}^{2+}$  current was measured in  $N = 7$  cells tested with this protocol (Fig. 12B). Since  $\text{Na}_v1.2$  is permeable to  $\text{Ca}^{2+}$  (Fig. 6), this result indicates that attX affects the kinetics of inactivation of  $\text{Na}_v1.6$ , but also that this VGNC isoform is not contributing to the early  $\text{Ca}^{2+}$  influx. We concluded that only  $\text{Na}_v1.2$  mediates  $\text{Ca}^{2+}$  influx during

the generating AP in the AIS and that only this isoform is functionally coupled to BK CAKCs.

### The $\text{Na}_v1.2$ -BK channel interaction is mimicked by simulations in a NEURON model

To mimic the experimental AP generation in the AIS, we built a NEURON model on the basis of our dataset.

Starting from the model reported in Hallermann et al. (2012) and already utilized in our previous article (Filipis & Canepari, 2021), we adapted the AIS morphology to the mouse L5 pyramidal neuron and replaced the  $\text{Na}_v1.2$  and  $\text{Na}_v1.6$  channel models with those proposed in Mainen et al. (1995), distributed consistently with the results reported by Hu et al. (2009; see Fig 13A). From this starting model, we modified the channel functions, as

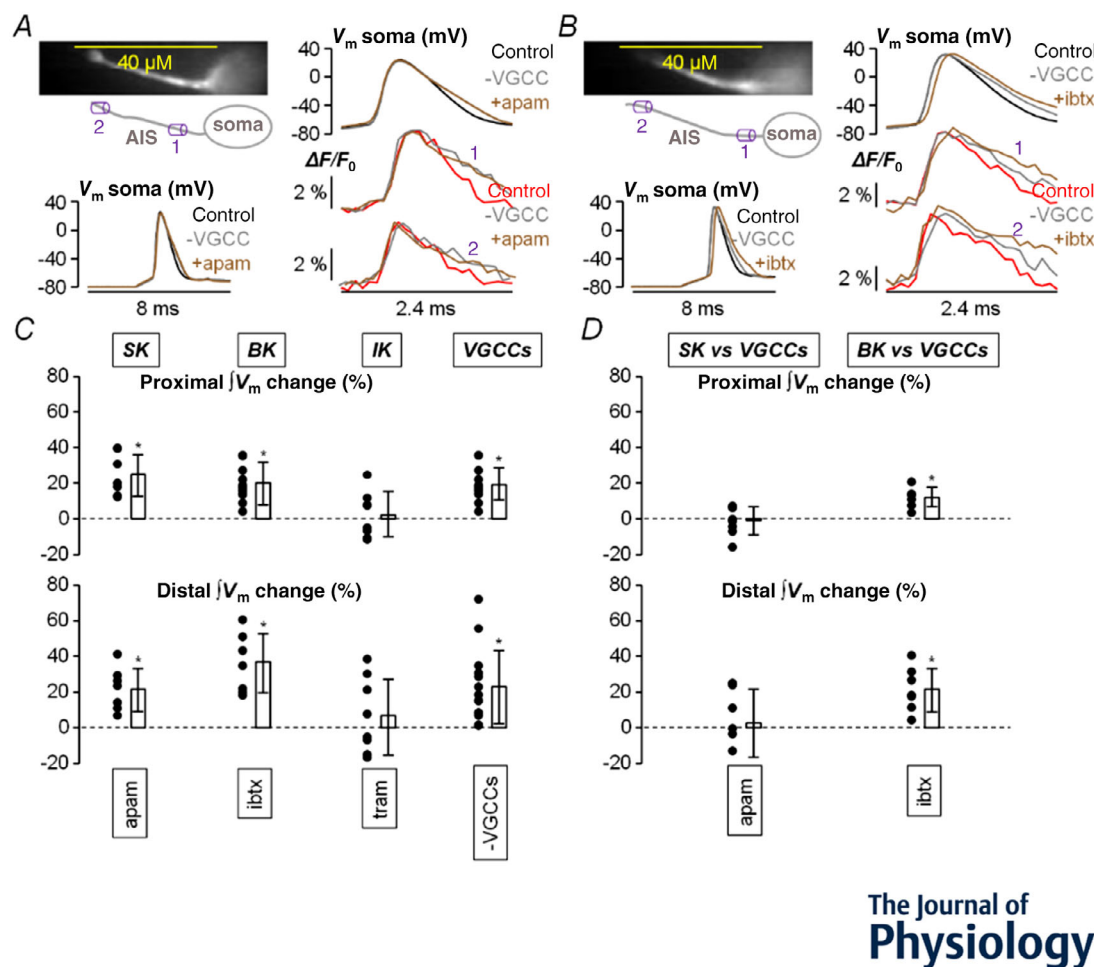


**Figure 8.** Effect of blocking SK CAKCs or BK CAKCs on the AP waveform in the AIS, after blocking VGCCs

A, left, fluorescence image (JPW1114) of the AIS and its reconstruction with a proximal region (1) and a distal (2) region indicated; somatic AP before and after sequentially blocking first VGCCs (grey trace) only and then VGCCs and SK CAKCs with additional apamin (brown trace, superimposed on the grey trace). Right, somatic AP and associated  $V_m$  transients in 1 and 2 in control solution and after sequentially blocking first VGCCs only and then VGCCs and SK CAKCs with additional apamin. B, in another cell, same protocol as in A but by sequentially blocking first VGCCs only and then VGCCs and BK CAKCs with additional iberiotoxin. C, top, single values and percentage change of the proximal  $fV_m$  signal maximum after delivering apamin (SK,  $N = 7$  cells, mean  $\pm$  SD =  $24.7 \pm 11.7$ ), iberiotoxin (BK,  $N = 7$  cells, mean  $\pm$  SD =  $20.1 \pm 11.9$ ), tram-34 (IK,  $N = 8$  cells, mean  $\pm$  SD =  $2.2 \pm 12.7$ ) or the cocktail of VGCCs blockers ( $N = 14$  cells, mean  $\pm$  SD =  $19.0 \pm 8.9$ ). Bottom, in the same cells, single values and percentage change of the distal  $fV_m$  signal maximum after delivering apamin (mean  $\pm$  SD =  $21.7 \pm 12.0$ ), iberiotoxin (mean  $\pm$  SD =  $36.9 \pm 16.6$ ), tram-34 (mean  $\pm$  SD =  $6.7 \pm 21.1$ ) or the cocktail of VGCC blockers (mean  $\pm$  SD =  $22.9 \pm 20.5$ ). D, top, with respect to the block of VGCCs, single values and percentage change of the proximal  $fV_m$  signal maximum after delivering apamin ( $N = 7$  cells, mean  $\pm$  SD =  $-2.1 \pm 7.9$ ) or iberiotoxin ( $N = 7$  cells, mean  $\pm$  SD =  $12.1 \pm 5.4$ ). Bottom, in the same cells, single values and percentage change of the distal  $fV_m$  signal maximum after delivering apamin (mean  $\pm$  SD =  $2.4 \pm 19.1$ ) or iberiotoxin (mean  $\pm$  SD =  $21.5 \pm 12.2$ ). An asterisk indicates a significant change ( $*P < 0.01$ , paired  $t$  test). [Colour figure can be viewed at [wileyonlinelibrary.com](http://wileyonlinelibrary.com)]



described in the Methods, to match the experimental  $\text{Na}^+$  and  $V_m$  signals in the AIS. We then introduced  $\text{Ca}^{2+}$  permeability to  $\text{Na}_v1.2$  corresponding to 0.4% with respect to the permeability for  $\text{Na}^+$  (as suggested by Hanemaaijer et al., 2020) and we introduced an LVAC an HVAC. We introduced an endogenous  $\text{Ca}^{2+}$  buffer and, when matching  $\text{Ca}^{2+}$  imaging experiments only, a  $\text{Ca}^{2+}$  buffer corresponding to 2 mM OG5N. Finally, we introduced SK and BK CAKCs and we explicitly introduced a coupling

between SK channels and LVACs as described in the Methods. The relative spatial distributions of VGNCs, VGCCs, and BK and SK channels, reported in Fig 13A, were set in order to reproduce the experimental results. Fig. 13B shows the proximal and distal  $V_m$  waveforms, the  $\text{Na}^+$  transients and the  $\text{Ca}^{2+}$  transients obtained by running computer simulations with the NEURON model. To validate the ability of the model to match the experimental evidence, we simulated the block of 80% VGCCs, of 80% SK channels (experiments with apamin) or of 80% BK channels (experiments with iberiotoxin). As shown in Fig. 13C, computer simulations qualitatively replicate the experimental changes of the AP shape reported in Fig. 7, indicating that the model realistically reproduces the activation of CAKCs during AP generation. Thus, we eventually mimicked the effect of hwtx to produce a partial block of  $\text{Na}_v1.2$  that replicates the experimental shift of the AP with minimal change of the peak and the reduction of the global  $\text{Na}^+$  transient of  $\sim 30\%$  (see Fig. 3). As shown in Fig 13D, the simulation reproduces the experimental reduction of the  $\text{Na}^+$  and  $\text{Ca}^{2+}$  transients and, more importantly, the widening of the distal AP (see Fig. 4). Thus, the NEURON model that we built predicts the interplay between  $\text{Na}_v1.2$  and BK CAKCs associated with the generation of the AP in the AIS and replicates, in a computer simulation, the experimental widening of the axonal AP produced by hwtx delivery.

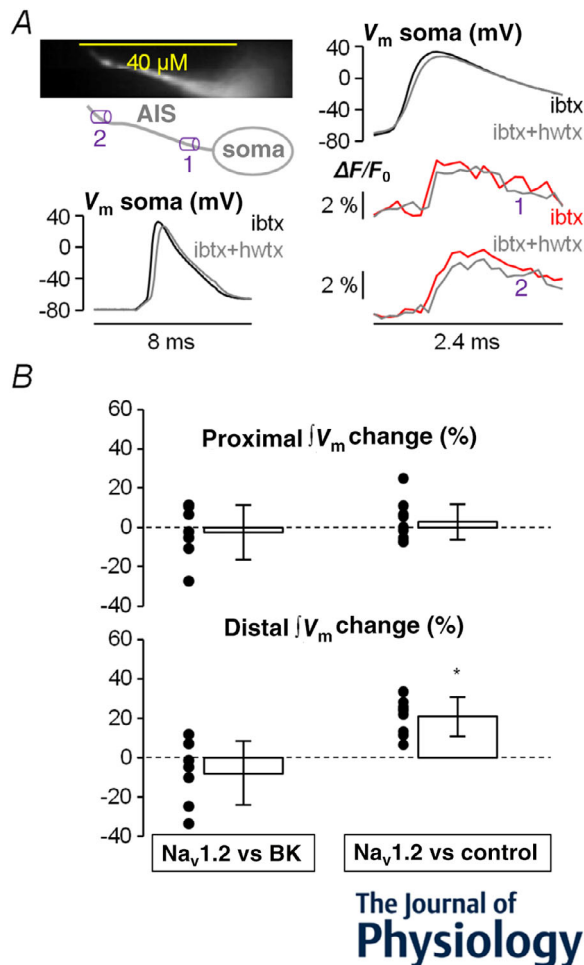


**Figure 9.** Effect of hwtx on the AP waveform in the AIS after blocking BK channels

A, left, fluorescence image (JPW1114) of the AIS and its reconstruction with a proximal region (1) and a distal region (2) indicated; somatic AP before and after locally delivering 80 nM hwtx in the presence of iberiotoxin (1  $\mu\text{M}$ ) reported below. Right, somatic AP and associated  $V_m$  transients in 1 and 2 in the presence of iberiotoxin before and after hwtx delivery. B, single cell values and percentage change ( $N = 7$  cells) of the  $fV_m$  signal maximum after locally delivering hwtx in the presence of iberiotoxin in proximal regions (mean  $\pm$  SD =  $-2.3 \pm 13.8$ ), and in distal regions (mean  $\pm$  SD =  $-7.9 \pm 16.3$ ). The statistics of the  $fV_m$  signal maximum after locally delivering hwtx in control solution (Fig. 4C) are also reported for comparison on the right. An asterisk indicates a significant change ( $*P < 0.01$ , paired  $t$  test). [Colour figure can be viewed at [wileyonlinelibrary.com](http://wileyonlinelibrary.com)]

### BK CAKCs can be slightly activated by $\text{Na}_v1.2$ VGNCs in HEK293 cells

We finally explored the question of whether  $\text{Na}_v1.2$  can activate BK CAKCs in non-physiological contexts. For this, we performed patch clamp recordings in  $N = 12$  HEK293- $\text{Na}_v1.2$  cells co-expressing BK CAKCs. Cells in voltage clamp mode were stimulated by changing the holding potential from  $-80$  to  $0$  mV with a pulse of 20 ms duration (Fig. 14A). In all cells tested, an outward current  $> 1$  nA was observed. This current was boosted when changing the extracellular  $\text{Ca}^{2+}$  concentration from 1 to 4 mM (green trace in Fig. 14A) and it was not blocked by perfusion with 1  $\mu\text{M}$  of the VGNC blocker tetrodotoxin (TTX, red trace in Fig. 14A). In contrast, the current was strongly inhibited by perfusion with 300 nM of the BK CAKC blocker iberiotoxin (ibtx, Fig. 14B). These results are consistent with a recent report demonstrating that  $\text{Ca}_v1.2$  (L-type VGCCs) are endogenously expressed in HEK293 cells (Archana et al., 2022) and this VGCC is known to activate BK CAKCs in a heterologous system (Berkefeld et al., 2013).  $\text{Na}_v1.2$  and L-type VGCCs, however, have very different kinetics of inactivation and recovery from inactivation. Thus, as shown in Fig. 14C, we applied a stimulating protocol consisting of a train of 10 stimulating pulses at 20 Hz, in control condition (at 4 mM



extracellular  $\text{Ca}^{2+}$ ) and after perfusing with  $1 \mu\text{M}$  TTX. In the cell illustrated in Fig. 14C, the fast ( $\sim 2$  ms duration) inward current in control conditions was progressively inactivated reaching, at the 6th pulse, a value that was  $\sim 20\%$  of the value of the 1st pulse (traces on the left). In contrast, in the presence of TTX, the initial part of the current was nearly identical for the 10 pulses (traces on the right). Thus, we subtracted from the first current the five last currents of the train. The first example of Fig. 14D (cell 1) shows the 8th current subtracted from the 1st current from the cell of Fig. 14C. Both in control and in the presence of TTX, the traces were characterized by large fluctuations in channel noise, but only in the control case did the build-up of these fluctuations produce a detectable outward current. This phenomenon was observed in other four cells tested in this way (cells 2–5, Fig. 14D). Thus, to analyse the outward current difference in the absence of the channel noise, we applied a 200 Hz median filter

(upper traces in Fig. 14D) and calculated the averaged current during the last 16 ms of the pulse over the last five pulses of the train. In the five cells analysed, the averaged outward current of  $105 \pm 23$  pA observed in control conditions dropped to  $7 \pm 21$  pA when the same cells were perfused with TTX and this change was significant ( $P = 1.08 \times 10^{-4}$ , paired  $t$  test, Fig. 14E). This result demonstrates that, although the majority of BK CAKC was activated by L-type VGCCs in HEK293 cells, a small but significant TTX-dependent outward current was present, indicating that BK CAKCs can be partially activated by  $\text{Na}_v1.2$  in this heterologous system.

## Discussion

If co-expression of multiple isoforms of VGNCs occurs in the mammalian AIS, does each isoform carry one or more

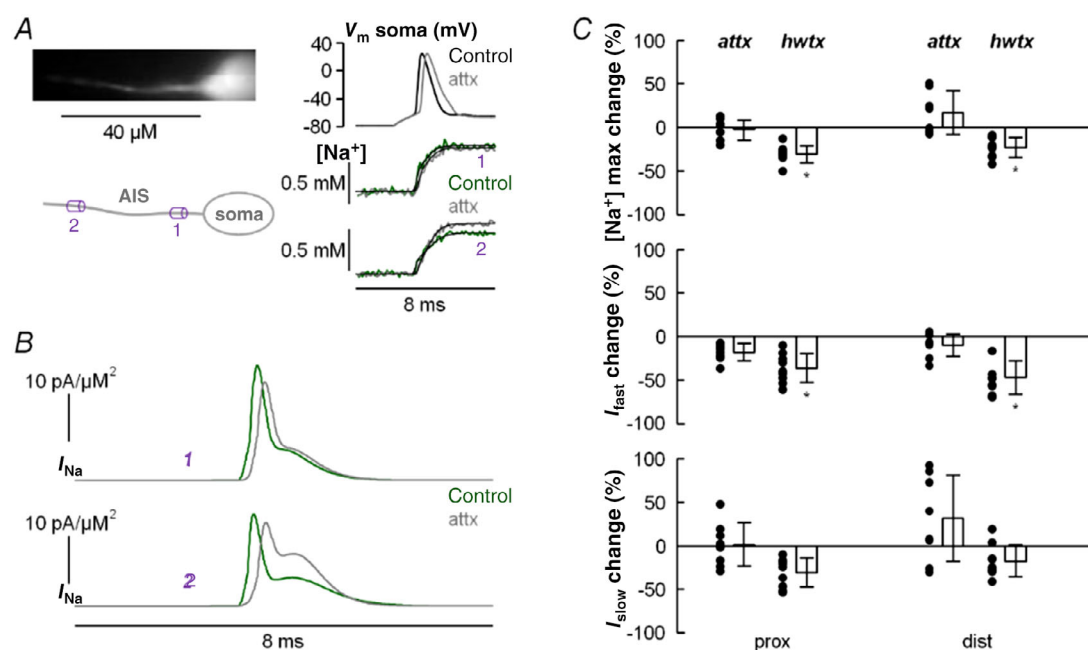


**Figure 10. Analysis of the effect of 4,9-anhydrotetrodotoxin (attx) on the  $\text{Na}^+$  influx in the AIS**

A, left, fluorescence image ( $\text{Na}^+$  indicator ING-2) of the AIS and its reconstruction with a proximal region (1) and a distal (2) region indicated. Right, somatic AP in control solution and after locally delivering 800 nM attx (top) and associated corrected  $\text{Na}^+$  transients fitted with a model function in 1 and 2. B, from the experiment in A,  $\text{Na}^+$  currents calculated from the time-derivative of the  $\text{Na}^+$  transient fits. C, top, percentage change of the  $\text{Na}^+$  transient maximum after addition of attx ( $N = 8$  cells) in proximal regions (mean  $\pm$  SD =  $-1.9 \pm 11.6$ ), and in distal regions (mean  $\pm$  SD =  $16.8 \pm 24.8$ ); the values and statistics of the equivalent experiments with hwtx (Fig. 3) are reported for comparison. Middle, percentage change of the fast component of the  $\text{Na}^+$  current ( $I_{\text{fast}}$ ) after addition of attx in proximal regions (mean  $\pm$  SD =  $-17.9 \pm 9.9$ ), and in distal regions (mean  $\pm$  SD =  $10.2 \pm 13.1$ ); the values and statistics of the equivalent experiments with hwtx are reported for comparison. Bottom, percentage change of the slow component of the  $\text{Na}^+$  current ( $I_{\text{slow}}$ ) after addition of attx in proximal regions (mean  $\pm$  SD =  $1.4 \pm 25.2$ ), and in distal regions (mean  $\pm$  SD =  $31.5 \pm 49.4$ ); the values and statistics of the equivalent experiments with hwtx (Fig. 3C) are reported for comparison; an asterisk indicates a significant change ( $*P < 0.01$ , paired  $t$  test). [Colour figure can be viewed at [wileyonlinelibrary.com](http://wileyonlinelibrary.com)]

specific roles in the generation and propagation of the AP? In pyramidal neurons, the different temporal and spatial patterns of expression of  $\text{Na}_v1.2$  and  $\text{Na}_v1.6$ , but also the diverse biophysical properties underlying activation and inactivation, suggest that these two channels contribute differently to the generation/propagation of APs (Hu et al., 2009), as well as to the ability to mediate high- or low-frequency firing (Rush et al., 2005). In the present study, we demonstrate that the exclusive permeability of  $\text{Na}_v1.2$  to  $\text{Ca}^{2+}$  (Hanemaaijer et al., 2020) allows activation of BK CAKCs in the AIS, as predicted on the basis of biophysical properties of the channel. In

this way, the interplay between  $\text{Na}_v1.2$ , mediating the AP rise, and BK channels regulating the peak and the early phase of the AP repolarization, shapes the AP waveform at the site of generation. To reach this important conclusion, we combined ultrafast imaging techniques with pharmacological analyses using selective channel blockers. The most important molecule used in this study was  $\text{G}^1\text{G}^4$ -huwentoxin-IV, mutated from huwentoxin-IV, a peptide from the Chinese bird spider *Haplopelma schmidtii* (Xiao et al., 2011). Using this potent  $\text{Na}_v1.2$  inhibitor, sufficiently selective against  $\text{Na}_v1.6$ , we could block, in a reliable manner, 30–40% of  $\text{Na}_v1.2$

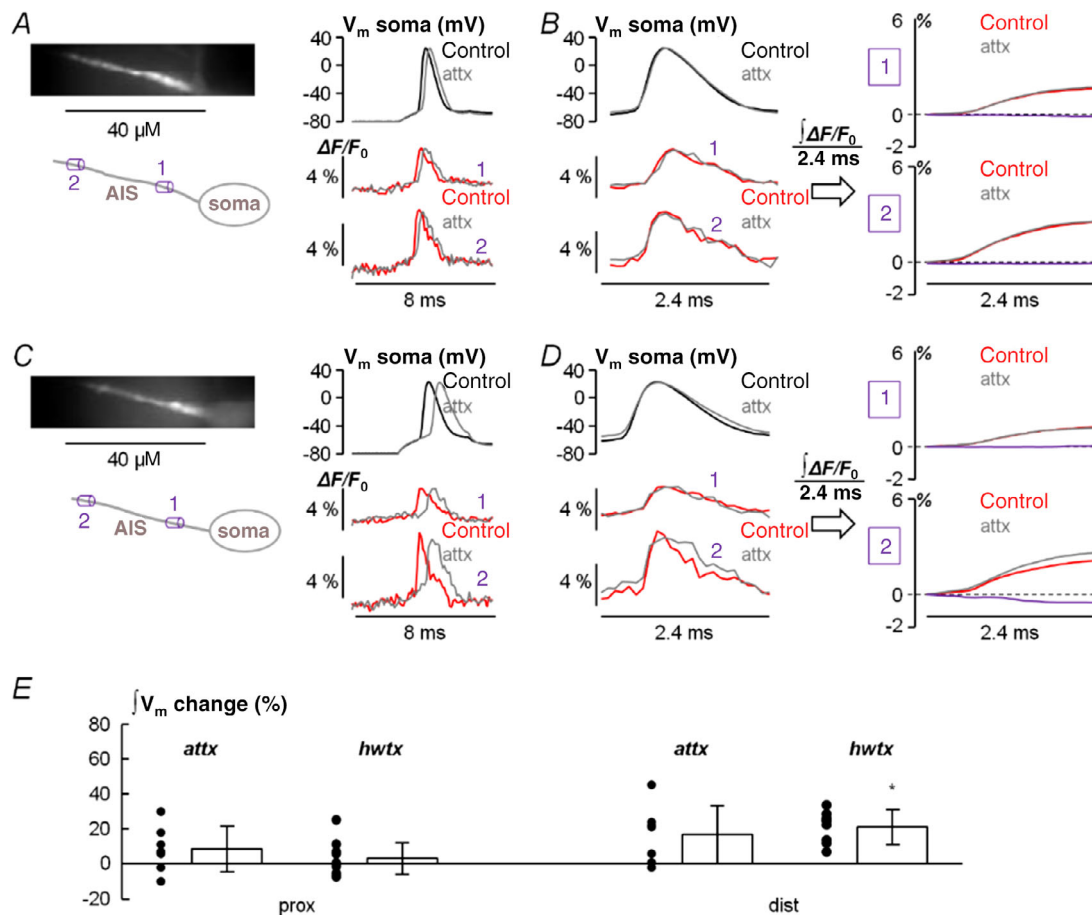


**Figure 11. Analysis of the effect of *attx* on the AP waveform in the AIS**

A, left, fluorescence image (JPW1114) of the AIS and its reconstruction with a proximal region (1) and a distal (2) region indicated. Right, somatic AP in control solution and after locally delivering 800 nM *attx* (top) and associated  $V_m$  transients in 1 and 2. B, left, somatic and axonal APs at a different time scale (2.4 ms duration). Right, quantification of the AP waveform shape by calculation of  $V_m$  integral ( $fV_m$ ) over the 2.4 ms time window comprising the AP signal. In this cell, the local delivery of *attx* does not change the waveform of the axonal AP. C and D, same as A and B in another cell where the local delivery of *attx* widens the waveform of the axonal AP at the distal site. E, percentage change of the  $fV_m$  signal maximum after delivery of *attx* ( $N = 7$  cells) in proximal regions (mean  $\pm$  SD =  $8.6 \pm 13.1$ ), and in distal regions (mean  $\pm$  SD =  $16.7 \pm 16.5$ ); the values and statistics of the equivalent experiments with *hwtx* (Fig. 4C) are reported for comparison; an asterisk indicates a significant change ( $*P < 0.01$ , paired  $t$  test). [Colour figure can be viewed at [wileyonlinelibrary.com](http://wileyonlinelibrary.com)]

in the AIS of L5 pyramidal neurons. This permitted detailed investigation of  $\text{Na}^+$  currents,  $V_m$  waveforms and  $\text{Ca}^{2+}$  currents, associated with the generating AP, in the AIS. We then analysed the change in AP waveform produced by selectively blocking different types of CAKCs, eventually establishing the interaction between  $\text{Na}_v1.2$  and BK channels. While this interaction was predicted in the recent past (Hanemaaijer et al., 2020), VGCCs have thus far been considered the principal activators of BK CAKCs in the majority of cellular systems (Berkefeld et al., 2010). Thus, in a series of additional experiments, we co-expressed  $\text{Na}_v1.2$  and BK channels in a HEK293 cell line and assessed the activation of BK CAKCs by brief depolarizing pulses. We found that in this heterologous system, BK CAKCs are mostly activated by endogenous  $\text{Ca}^{2+}$  channels (Archana et al., 2022), but a small TTX-dependent component of the outward current could be still detected, indicating the ability of  $\text{Na}_v1.2$  to activate BK channels. This result suggests that this functional coupling may in principle occur

also in other native cellular systems, but it can play a significant role only where the  $\text{Na}_v1.2$  component of the  $\text{Ca}^{2+}$  current is not negligible. In the AIS, several other channels contribute to the early process of generation and propagation of the AP. In particular, characterization of the somatic AP shape has revealed the role of multiple  $\text{K}^+$  channels (Pathak et al., 2016; Schwindt et al., 1988) and VGCCs (Pineda et al., 1998) in the various phases of AP repolarization. Thus, we created a NEURON model that adds to previous models developed for the AIS of L5 pyramidal neurons (Baranauskas et al., 2013; Cohen et al., 2020; Fleidervish et al., 2010; Hallermann et al., 2012; Hanemaaijer et al., 2020; Hu et al., 2009; Kole et al., 2008) and that reproduces our experimental results. Using this model, we were able to simulate the functional interaction between  $\text{Na}_v1.2$  and BK channels and mimic the experimental results obtained by blocking  $\text{Na}_v1.2$  with  $\text{G}^1\text{G}^4$ -huwentoxin-IV.

The process of AP generation starts with a sub-threshold depolarization that spreads from the soma (or physiologically from the dendrites through the soma) to the AIS. The observation of an early subthreshold component of the  $\text{Na}^+$  influx (Filipis & Canepari, 2021) indicates that VGNCs also contribute to amplify the axonal depolarization before AP onset (Goldwyn et al., 2019). Whereas the threshold for AP initiation is largely determined by  $\text{Na}_v1.6$  (Royeck et al., 2008), our results point to a major contribution of  $\text{Na}_v1.2$  in the  $\text{Na}^+$  current during the rising phase of the AP, in particular at its peak occurring at the AP upstroke, even in the distal sites of the AIS where  $\text{Na}_v1.6$  expression is dominant. Importantly, an early  $\text{Ca}^{2+}$  current occurring with kinetics similar to that of the  $\text{Na}^+$  current allows  $\text{Ca}^{2+}$  binding to its targets before the AP reaches its peak. This is crucial because BK CAKCs require concomitant  $\text{Ca}^{2+}$  binding and depolarization in order to open (Cui et al., 2009). At the peak of the AP, BK channels contribute substantially to the total  $\text{K}^+$  current that counterbalances the non-inactivated  $\text{Na}^+$  current, together with the diverse voltage-gated  $\text{K}^+$  channels expressed in the AIS (Trimmer, 2015). Thus, a decrease of the  $\text{Na}_v1.2$  current is counterbalanced by a decrease of the BK current, resulting in widening of the early phase of AP repolarization with a modest change of the AP peak. The interplay between  $\text{Na}_v1.2$  and BK channels is therefore a major determinant of the AP peak and a key regulator of the AP shape. After the peak, other channels contribute to the shape of the AP repolarization, in particular VGCCs and SK CAKCs. Our results also provide evidence of the precise role of these channels in shaping of the AP.

After generation, the AP propagates along the axonal branches and regenerates at Ranvier nodes, and the waveform at synaptic terminals regulates neurotransmitter release providing an analogue modulation of synaptic transmission (Rama et al., 2018). The AP from the AIS also

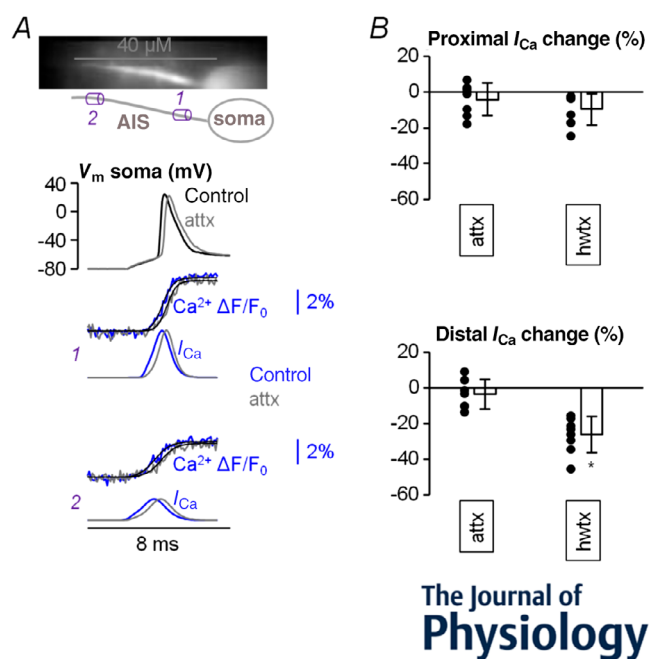


**Figure 12. Analysis of the effect of attx on the  $\text{Ca}^{2+}$  influx in the AIS**

**A**, top,  $\text{Ca}^{2+}$  fluorescence image (OG5N) of the AIS and its reconstruction with a proximal region (1) and a distal (2) region indicated. Bottom, somatic AP and associated  $\text{Ca}^{2+}$  transients and currents in 1 and 2 in control solution and after locally delivering 800 nM attx. **B**, top, single values and percentage change of the proximal  $\text{Ca}^{2+}$  current peak after addition of attx ( $N = 7$  cells, mean  $\pm$  SD =  $-4.5 \pm 9.2$ ). Right, in the same cells, single values and percentage change of the distal  $\text{Ca}^{2+}$  current peak after addition of attx (mean  $\pm$  SD =  $-3.6 \pm 8.3$ ); the values and statistics of the equivalent experiments with hwtx (Fig. 6A) are reported for comparison; an asterisk indicates a significant change ( $*P < 0.01$ , paired  $t$  test). [Colour figure can be viewed at [wileyonlinelibrary.com](http://wileyonlinelibrary.com)]

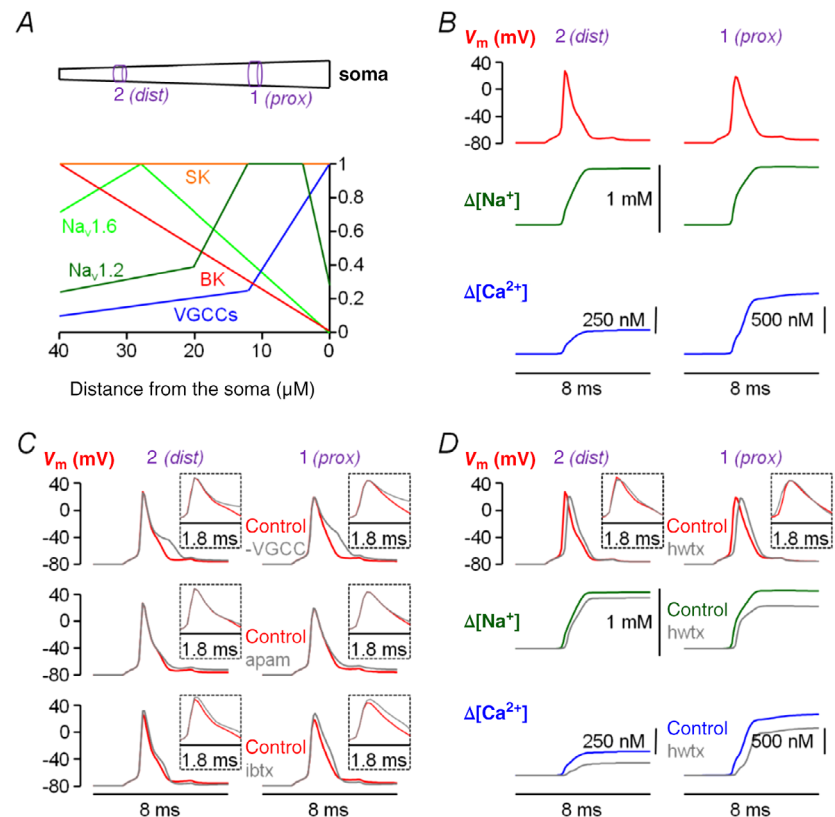
back-propagates to the soma and then along the dendrites, progressively changing its shape and regulating synaptic integration (Gulledge et al., 2005). Eventually, the AP waveform in the AIS sets the way in which a neuron can respond to prolonged depolarization by firing several APs at high frequencies, determining the ability of the neuron to encode signals (Kole & Stuart, 2012). The shape of the AP at its site of origin is therefore the starting point of the consequent physiological processes occurring at the other sites of the cells. First, the AP waveform, modulated during propagation along the axons, regulates neurotransmitter release and therefore synaptic transmission at synaptic terminals, in this way providing an analogue component of the digital information process (Rama et al., 2015). Second, the AP waveforms regulate neuronal firing. Interestingly, in CA1 hippocampal pyramidal neurons, it has been shown that BK CAKCs facilitate high-frequency firing and cause early spike frequency adaptation (Gu et al., 2007). Regulation of the firing frequency is crucial for coupling among the different sites of the cell that are believed to underlie conscious processing (Aru et al., 2020) and, in L5 pyramidal neurons, high-frequency bursts of APs back-propagate along the

apical dendrite reaching the tuft and provoking  $\text{Ca}^{2+}$  electrogenesis (Larkum et al., 1999). Finally, neurons with sharper AP kinetics have been correlated with human individuals exhibiting high IQ scores (Goriounova et al., 2018).

The AIS regulates the trafficking and distribution of proteins that function in somatodendritic or axonal compartments, and genetic mutations in this neuronal part may cause neurological disorders (Huang & Rasband, 2018). The result reported in this study is therefore a potential key to interpretation in the investigation of the variety of neurological disorders associated with critical mutations of  $\text{Na}_v1.2$  (Crawford et al., 2021; Meisler et al., 2021) or BK channels (Bailey et al., 2019). Among the hundreds of mutations of the *SCN2A* gene, encoding  $\text{Na}_v1.2$ , those classified as 'gain of function' are typically associated with mild epilepsy (Heron et al., 2002), or with severe epileptic encephalopathies (Wolff et al., 2019). These phenotypes are generally explained by an enhancement of activity of glutamatergic neurons, despite  $\text{Na}_v1.2$  also being expressed in GABAergic interneurons (Li et al., 2014). The range of neurological disorders associated with

### Figure 13. NEURON simulations of the AP generation in the AIS

A, top, structure of the AIS (40  $\mu\text{m}$  long) with proximal (1) compartment and distal (2) compartment at 10–12 and 30–32  $\mu\text{m}$  from the soma, respectively. Bottom, normalized distributions of  $\text{Na}_v1.2$  VGNCs (dark green),  $\text{Na}_v1.6$  VGNCs (light green), VGCCs (blue), SK CAKCs (orange) and BK CAKCs (red) along the AIS. B,  $V_m$  (AP waveform), free  $\text{Na}^+$  and free  $\text{Ca}^{2+}$  from a computer simulation of the NEURON model in the proximal and distal regions. The presence of OG5N was taken into account for the free  $\text{Ca}^{2+}$  estimate. C,  $V_m$  (AP waveform) from computer simulations of the NEURON model in the proximal and distal regions in control conditions and after mimicking the delivery of VGCC blockers (80% reduction in VGCCs, top trace), of apamin (80% reduction in SK CAKCs, middle trace) or of iberiotoxin (80% reduction in BK CAKCs, bottom trace). The changes of the AP waveform are reported in the insets. The simulations qualitatively reproduce the experimental results reported in Fig. 7. D,  $V_m$  (AP waveform), free  $\text{Na}^+$  and free  $\text{Ca}^{2+}$  from computer simulations of the NEURON model in the proximal and distal regions in control conditions and after mimicking the delivery of hwtx. The presence of OG5N was taken into account for the free  $\text{Ca}^{2+}$  estimate. The changes of the AP waveform are reported in the insets. The simulations qualitatively reproduce the experimental results reported in Figs 3, 4 and 6. [Colour figure can be viewed at [wileyonlinelibrary.com](http://wileyonlinelibrary.com)]





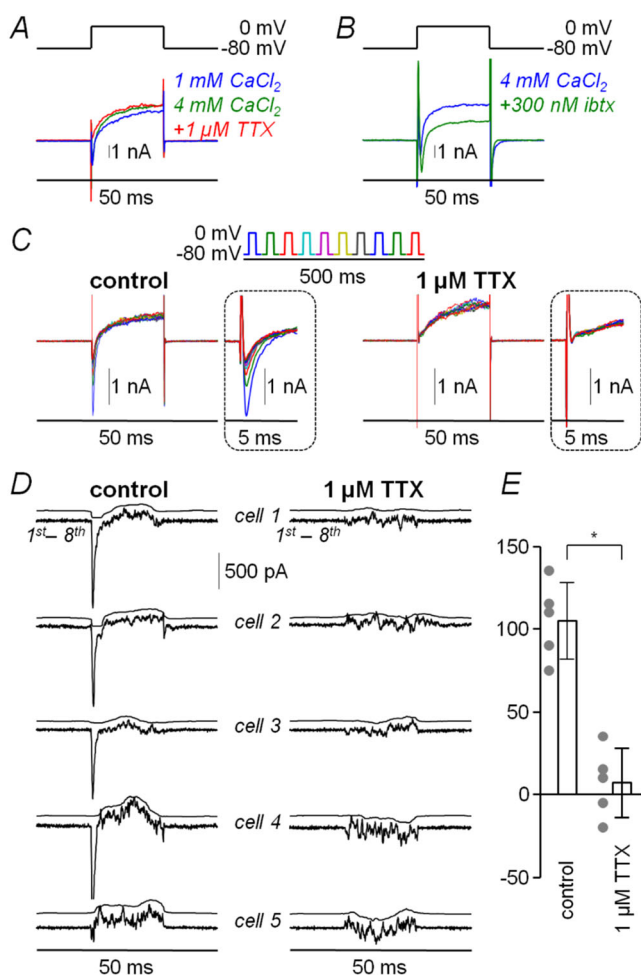


**Figure 14.** Analysis of the BK CAKC current in HEK293 cells co-expressing Na<sub>v</sub>1.2

A, top, stimulating pulse (20 ms duration from  $-80$  to  $0$  mV). Bottom, current recorded in HEK293 cell co-expressing Na<sub>v</sub>1.2 and BK CAKCs in the presence of  $1$  mM extracellular CaCl<sub>2</sub> (blue trace), in the presence of  $4$  mM extracellular CaCl<sub>2</sub> (blue trace), and after perfusing with  $1$   $\mu$ M TTX (red trace). B, same as in A in another cell where the blue trace is in the presence of  $4$  mM extracellular CaCl<sub>2</sub> and the green trace is after perfusing with  $300$  nM of the BK CAKC blocker iberiotoxin (ibtx). C, top, stimulating train of  $10$  pulses at  $20$  Hz where each colour indicates the traces corresponding to a pulse. Bottom-left, currents recorded in each pulse in the presence of  $4$  mM (control) extracellular CaCl<sub>2</sub> with zoom of the first milliseconds in the inset; the inward current is progressively inactivated during the train. Bottom-right, same as bottom-left but after perfusing with TTX; no inactivation is observed under this condition. D, difference between the 1st current and the 8th current in five cells (cell 1 is the same as in B) in control condition (left) and after perfusing with TTX; the recording after applying a  $200$  Hz median filter is reported on the top of each trace. E, filtered outward current difference averaged during the last  $16$  ms of the pulse over the five last pulses of the train in the five cells of D. The mean  $\pm$  SD of these cells, both in control condition and after perfusing with TTX, is also reported. An asterisk indicates a significant change ( $P = 1.08 \times 10^{-4}$ , paired  $t$  test) of the outward filtered current difference. [Colour figure can be viewed at [wileyonlinelibrary.com](http://wileyonlinelibrary.com)]

other Na<sub>v</sub>1.2 mutations is far more complex, including autism and intellectual disability (Meisler et al., 2021). In parallel, heterogeneous combinations of disorders including seizure and intellectual disability are associated with mutations of KCNMA-1, the gene encoding BK channels (Bailey et al., 2019). Thus, the functional link between Na<sub>v</sub>1.2 and BK channels can represent an element to unravel the complexity of these channelopathies using murine models. In a heterozygote SCN2A knock-out mouse, haploinsufficiency of Na<sub>v</sub>1.2 is associated with an autistic-like phenotype attenuated with age (Léna & Mantegazza, 2019), but in another SCN2A<sup>+/-</sup> model the phenotype is also characterized by epileptic seizures (Miyamoto et al., 2019) consistent with hyperexcitability of L5 pyramidal neurons (Spratt et al., 2021). More recently, a mouse model carrying the K1422A mutation in the SCN2A gene has been generated (Echevarria et al., 2021). This specific mutation is characterized by an increase in Ca<sup>2+</sup> permeability of Na<sub>v</sub>1.2 and a mix of phenotypes including rare seizures. This is an example where the result reported in the present study can represent an important key in interpretation to link the cellular mechanisms to the behavioural dysfunction in the mouse model.

## References

- Ait Ouares, K., & Canepari, M. (2020). The origin of physiological local mGluR1 Supralinear Ca<sup>2+</sup> signals in Cerebellar Purkinje Neurons. *Journal of Neuroscience*, **40**(9), 1795–1809.
- Ait Ouares, K., Filipis, L., Tzilivaki, A., Poirazi, P., & Canepari, M. (2019). Two distinct sets of Ca<sup>2+</sup> and K<sup>+</sup> channels are activated at different membrane potentials by the climbing fiber synaptic potential in Purkinje Neuron Dendrites. *Journal of Neuroscience*, **39**(11), 1969–1981.
- Ait Ouares, K., Jaafari, N., & Canepari, M. (2016). A generalised method to estimate the kinetics of fast Ca(2+) currents from Ca(2+) imaging experiments. *Journal of Neuroscience Methods*, **268**, 66–77.
- Archana, G. M., Arunkumar, R. C., & Omkumar, R. V. (2022). Assays for L-type voltage gated calcium channels. *Analytical Biochemistry*, **656**, 114827.
- Almog, M., & Korngreen, A. (2014). A quantitative description of dendritic conductances and its application to dendritic excitation in layer 5 pyramidal neurons. *Journal of Neuroscience*, **34**(1), 182–196.
- Aru, J., Suzuki, M., & Larkum, M. E. (2020). Cellular mechanisms of conscious processing. *Trends in Cognitive Sciences*, **24**(10), 814–825.
- Astman, N., Gutnick, M. J., & Fleidervish, I. A. (2006). Persistent sodium current in layer 5 neocortical neurons is primarily generated in the proximal axon. *Journal of Neuroscience*, **26**(13), 3465–3473.
- Bailey, C. S., Moldenhauer, H. J., Park, S. M., Keros, S., & Meredith, A. L. (2019). KCNMA1-linked channelopathy. *Journal of General Physiology*, **151**(10), 1173–1189.

- Baranauskas, G., David, Y., & Fleidervish, I. A. (2013). Spatial mismatch between the Na<sup>+</sup> flux and spike initiation in axon initial segment. *Proceedings National Academy of Science USA*, **110**(10), 4051–4056.
- Bean, B. P. (2007). The action potential in mammalian central neurons. *Nature Reviews Neuroscience*, **8**(6), 451–465.
- Berkefeld, H., & Fakler, B. (2013). Ligand-gating by Ca<sup>2+</sup> is rate limiting for physiological operation of BK(Ca) channels. *Journal of Neuroscience*, **33**(17), 7358–7367.
- Berkefeld, H., Fakler, B., & Schulte, U. (2010). Ca<sup>2+</sup>-activated K<sup>+</sup> channels: From protein complexes to function. *Physiological Reviews*, **90**(4), 1437–1459.
- Blömer, L. A., Canepari, M., & Filipis, L. (2021). Ultrafast sodium imaging of the axon initial segment of neurons in mouse brain slices. *Current Protocols*, **1**(3), e64.
- Bosmans, F., Rash, L., Zhu, S., Diochot, S., Lazdunski, M., Escoubas, P., & Tytgat, J. (2006). Four novel tarantula toxins as selective modulators of voltage-gated sodium channel subtypes. *Molecular Pharmacology*, **69**(2), 419–429.
- Canepari, M., & Mammano, F. (1999). Imaging neuronal calcium fluorescence at high spatio-temporal resolution. *Journal of Neuroscience Methods*, **87**(1), 1–11.
- Cohen, C. C. H., Popovic, M. A., Klooster, J., Weil, M. T., Möbius, W., Nave, K. A., & Kole, M. H. P. (2020). Saltatory conduction along myelinated axons involves a periaxonal nanocircuit. *Cell*, **180**(2), 311–322.e15.
- Crawford, K., Xian, J., Helbig, K. L., Galer, P. D., Parthasarathy, S., Lewis-Smith, D., Kaufman, M. C., Fitch, E., Ganesan, S., O'Brien, M., Codoni, V., Ellis, C. A., Conway, L. J., Taylor, D., Krause, R., & Helbig, I. (2021). Computational analysis of 10,860 phenotypic annotations in individuals with SCN2A-related disorders. *Genetics in Medicine*, **23**(7), 1263–1272.
- Cui, J., Yang, H., & Lee, U. S. (2009). Molecular mechanisms of BK channel activation. *Cellular and Molecular Life Sciences*, **66**(5), 852–875.
- Delvendahl, I., Jablonski, L., Baade, C., Matveev, V., Neher, E., & Hallermann, S. (2015). Reduced endogenous Ca<sup>2+</sup> buffering speeds active zone Ca<sup>2+</sup> signaling. *Proceedings National Academy of Science USA*, **112**(23), 3075–3084.
- Echevarria-Cooper, D. M., Hawkins, N. A., Misra, S. N., Huffman, A., Thaxton, T., Thompson, C. H., Ben-Shalom, R., Nelson, A. D., Lipkin, A. M., George, A. L. Jr, Bender, K. J., & Kearney, J. A. (2021). Cellular and behavioral effects of altered Nav1.2 sodium channel ion permeability in Scn2a<sup>K1422E</sup> mice. *BioRxiv*. Advance online publication. <https://doi.org/10.1101/2021.07.19.452930>
- Filipis, L., Ait Ouare, K., Moreau, P., Tanese, D., Zampini, V., Latini, A., Bleau, C., Bleau, C., Graham, J., & Canepari, M. (2018). A novel multisite confocal system for rapid Ca<sup>2+</sup> imaging from submicron structures in brain slices. *Journal of Biophotonics*, **11**(3), e201700197.
- Filipis, L., & Canepari, M. (2021). Optical measurement of physiological sodium currents in the axon initial segment. *The Journal of Physiology*, **599**(1), 49–66.
- Fleidervish, I. A., Lasser-Ross, N., Gutnick, M. J., & Ross, W. N. (2010). Na<sup>+</sup> imaging reveals little difference in action potential-evoked Na<sup>+</sup> influx between axon and soma. *Nature Neuroscience*, **13**(7), 852–860.
- Goldwyn, J. H., Remme, M. W. H., & Rinzel, J. (2019). Soma-axon coupling configurations that enhance neuronal coincidence detection. *Plos Computational Biology*, **15**(3), e1006476.
- Goriounova, N. A., Heyer, D. B., Wilbers, R., Verhoog, M. B., Giugliano, M., Verbist, C., Obermayer, J., Kerkhofs, A., Smeding, H., Verberne, M., Idema, S., Baayen, J. C., Pieneman, A. W., de Kock, C. P., Klein, M., & Mansvelder, H. D. (2018). Large and fast human pyramidal neurons associate with intelligence. *Elife*, **7**, e41714.
- Gu, N., Vervaeke, K., & Storm, J. F. (2007). BK potassium channels facilitate high-frequency firing and cause early spike frequency adaptation in rat CA1 hippocampal pyramidal cells. *The Journal of Physiology*, **580**(3), 859–882.
- Gulledge, A. T., Kampa, B. M., & Stuart, G. J. (2005). Synaptic integration in dendritic trees. *Journal of Neurobiology*, **64**(1), 75–90.
- Hallermann S de Kock, C. P., Stuart, G. J., & Kole, M. H. (2012). State and location dependence of action potential metabolic cost in cortical pyramidal neurons. *Nature Neuroscience*, **15**(7), 1007–1014.
- Hanemaaijer, N. A., Popovic, M. A., Wilders, X., Grasman, S., Pavón Arocas, O., & Kole, M. H. (2020). Ca<sup>2+</sup> entry through Nav channels generates submillisecond axonal Ca<sup>2+</sup> signaling. *Elife*, **9**, e54566.
- Hedrich, U. B. S., Lauxmann, S., & Lerche, H. (2019). SCN2A channelopathies: Mechanisms and models. *Epilepsia*, **60**(3), S68–S76.
- Heron, S. E., Crossland, K. M., Andermann, E., Phillips, H. A., Hall, A. J., Bleasel, A., Shevell, M., Mercho, S., Seni, M. H., Guiot, M. C., Mulley, J. C., Berkovic, S. F., & Scheffer, I. E. (2002). Sodium-channel defects in benign familial neonatal-infantile seizures. *Lancet*, **360**(9336), 851–852.
- Hu, W., Tian, C., Li, T., Yang, M., Hou, H., & Shu, Y. (2009). Distinct contributions of Na(v)1.6 and Na(v)1.2 in action potential initiation and backpropagation. *Nature Neuroscience*, **12**(8), 996–1002.
- Huang, C. Y., & Rasband, M. N. (2018). Axon initial segments: Structure, function, and disease. *Annals of the New York Academy of Sciences*, **1420**(1), 46–61.
- Katz, E., Stoler, O., Scheller, A., Khrapunsky, Y., Goebbels, S., Kirchhoff, F., Gutnick, M. J., Wolf, F., & Fleidervish, I. A. (2018). Role of sodium channel subtype in action potential generation by neocortical pyramidal neurons. *Proceedings National Academy of Science USA*, **115**(30), 7184–7192.
- Kim, Y., Hsu, C. L., Cembrowski, M. S., Mensh, B. D., & Spruston, N. (2015). Dendritic sodium spikes are required for long-term potentiation at distal synapses on hippocampal pyramidal neurons. *Elife*, **4**, e06414.
- Kole, M. H., Ilschner, S., Kampa, B., Williams, S. R., Ruben, P. C., & Stuart, G. J. (2008). Action potential generation requires a high sodium channel density in the axon initial segment. *Nature Neuroscience*, **11**(2), 178–186.
- Kole, M. H., & Stuart, G. J. (2012). Signal processing in the axon initial segment. *Neuron*, **73**(2), 235–247.

- Jaafari, N., & Canepari, M. (2016). Functional coupling of diverse voltage-gated  $\text{Ca}^{2+}$  channels underlies high fidelity of fast dendritic  $\text{Ca}^{2+}$  signals during burst firing. *The Journal of Physiology*, **594**(4), 967–983.
- Jaafari, N., De Waard, M., & Canepari, M. (2014). Imaging fast calcium currents beyond the limitations of electrode techniques. *Biophysical Journal*, **107**(6), 1280–1288.
- Jaafari, N., Marret, E., & Canepari, M. (2015). Using simultaneous voltage and calcium imaging to study fast  $\text{Ca}^{2+}$  channels. *Neurophotonics*, **2**(2), 021010.
- Larkum, M. E., Kaiser, K. M., & Sakmann, B. (1999). Calcium electrogenesis in distal apical dendrites of layer 5 pyramidal cells at a critical frequency of back-propagating action potentials. *Proceedings National Academy of Science USA*, **96**(25), 14600–14604.
- Léna, I., & Mantegazza, M. (2019).  $\text{Na}_v1.2$  haploinsufficiency in *Scn2a* knock-out mice causes an autistic-like phenotype attenuated with age. *Scientific Reports*, **9**(1), 12886.
- Leterrier, C. (2016). The axon initial segment, 50 Years Later: A nexus for neuronal organization and function. *Current Topics in Membranes*, **77**, 185–233.
- Li, T., Tian, C., Scalmani, P., Frassoni, C., Mantegazza, M., Wang, Y., Yang, M., Wu, S., & Shu, Y. (2014). Action potential initiation in neocortical inhibitory interneurons. *Plos Biology*, **12**(9), e1001944.
- Lipkin, A. M., Cunniff, M. M., Spratt, P. W. E., Lemke, S. M., & Bender, K. J. (2021). Functional microstructure of  $\text{Ca}_v$ -mediated calcium signaling in the Axon initial segment. *Journal of Neuroscience*, **41**(17), 3764–3776.
- Lopez, L., Montnach, J., Oliveira-Mendes, B., Khakh, K., Thomas, B., Lin, S., Caumes, C., Wesolowski, S., Nicolas, S., Servent, D., Cohen, C., Bérout, R., Benoit, E., & De Waard, M. (2021). Synthetic analogues of Huwentoxin-IV spider peptide with altered human  $\text{Na}_v1.7/\text{Na}_v1.6$  selectivity ratios. *Frontiers in Cell and Developmental Biology*, **9**, 798588.
- Mahapatra, C., Brain, K. L., & Manchanda, R. A. (2018). biophysically constrained computational model of the action potential of mouse urinary bladder smooth muscle. *PLoS ONE*, **13**(7), e0200712.
- Mainen, Z. F., Joerges, J., Huguenard, J. R., & Sejnowski, T. J. (1995). A model of spike initiation in neocortical pyramidal neurons. *Neuron*, **15**(6), 1427–1439.
- Meisler, M. H., Hill, S. F., & Yu, W. (2021). Sodium channelopathies in neurodevelopmental disorders. *Nature Reviews Neuroscience*, **22**(3), 152–166.
- Menezes, L. F. S., Sabiá, E. F. Júnior, Tibery, D. V., Carneiro, L. D. A., & Schwartz, E. F. (2020). Epilepsy-related Voltage-gated sodium channelopathies: A review. *Frontiers in Pharmacology*, **11**, 1276.
- Migliore, M., Novara, G., & Tegolo, D. (2008). Single neuron binding properties and the magical number 7. *Hippocampus*, **18**(11), 1122–1130.
- Miyamoto, H., Tatsukawa, T., Shimohata, A., Yamagata, T., Suzuki, T., Amano, K., Mazaki, E., Raveau, M., Ogiwara, I., Oba-Asaka, A., Hensch, T. K., Itohara, S., Sakimura, K., Kobayashi, K., Kobayashi, K., & Yamakawa, K. (2019). Impaired cortico-striatal excitatory transmission triggers epilepsy. *Nature Communications*, **10**(1), 1917.
- Montnach, J., Blömer, L. A., Lopez, L., Filipis, L., Meudal, H., Lafoux, A., Nicolas, S., Chu, D., Caumes, C., Bérout, R., Jopling, C., Bosmans, F., Huchet, C., Landon, C., Canepari, M., & De Waard, M. (2022). In vivo spatiotemporal control of voltage-gated ion channels by using 1 photoactivatable peptidic toxins. *Nature Communications*, **13**(1), 417.
- Pathak, D., Guan, D., & Foehring, R. C. (2016). Roles of specific  $\text{K}_v$  channel types in repolarization of the action potential in genetically identified subclasses of pyramidal neurons in mouse neocortex. *Journal of Neurophysiology*, **115**(5), 2317–2329.
- Pineda, J. C., Waters, R. S., & Foehring, R. C. (1998). Specificity in the interaction of HVA  $\text{Ca}^{2+}$  channel types with  $\text{Ca}^{2+}$ -dependent AHPs and firing behavior in neocortical pyramidal neurons. *Journal of Neurophysiology*, **79**(5), 2522–2534.
- Popovic, M., Vogt, K., Holthoff, K., Konnerth, A., Salzberg, B. M., Grinvald, A., Antic, S. D., Canepari, M., & Zecevic, D. (2015). Imaging submillisecond membrane potential changes from individual regions of single axons, dendrites and spines. *Advances in Experimental Medicine and Biology*, **859**, 57–101.
- Rama, S., Zbili, M., Bialowas, A., Fronzaroli-Molinieres, L., Ankri, N., Carlier, E., Marra, V., & Debanne, D. (2015). Presynaptic hyperpolarization induces a fast analogue modulation of spike-evoked transmission mediated by axonal sodium channels. *Nature Communications*, **6**(1), 10163.
- Rama, S., Zbili, M., & Debanne, D. (2018). Signal propagation along the axon. *Current Opinion in Neurobiology*, **51**, 37–44.
- Roshchin, M. V., Ierusalimsky, V. N., Balaban, P. M., & Nikitin, E. S. (2020).  $\text{Ca}^{2+}$ -activated  $\text{KCa}_{3.1}$  potassium channels contribute to the slow afterhyperpolarization in L5 neocortical pyramidal neurons. *Scientific Reports*, **10**(1), 14484.
- Royeck, M., Horstmann, M. T., Remy, S., Reitze, M., Yaari, Y., & Beck, H. (2008). Role of axonal  $\text{Na}_v1.6$  sodium channels in action potential initiation of CA1 pyramidal neurons. *Journal of Neurophysiology*, **100**(4), 2361–2380.
- Rush, A. M., Dib-Hajj, S. D., & Waxman, S. G. (2005). Electrophysiological properties of two axonal sodium channels,  $\text{Nav}1.2$  and  $\text{Nav}1.6$ , expressed in mouse spinal sensory neurones. *The Journal of Physiology*, **564**(3), 803–815.
- Schwindt, P. C., Spain, W. J., Foehring, R. C., Stafstrom, C. E., Chubb, M. C., & Crill, W. E. (1988). Multiple potassium conductances and their functions in neurons from cat sensorimotor cortex in vitro. *Journal of Neurophysiology*, **59**(2), 424–449.
- Spratt, P. W. E., Alexander, R. P. D., Ben-Shalom, R., Sahagun, A., Kyoung, H., Keeshen, C. M., Sanders, S. J., & Bender, K. J. (2021). Paradoxical hyperexcitability from  $\text{Na}_v1.2$  sodium channel loss in neocortical pyramidal cells. *Cell Reports*, **36**(5), 109483.
- Spratt, P. W. E., Ben-Shalom, R., Keeshen, C. M., Burke, K. J. Jr, Clarkson, R. L., Sanders, S. J., & Bender, K. J. (2019). The Autism-associated gene *Scn2a* contributes to dendritic excitability and synaptic function in the prefrontal cortex. *Neuron*, **103**(4), 673–685.e5.

- Tian, C., Wang, K., Ke, W., Guo, H., & Shu, Y. (2014). Molecular identity of axonal sodium channels in human cortical pyramidal cells. *Frontiers in Cellular Neuroscience*, **8**, 297.
- Trimmer, J. S. (2015). Subcellular localization of K<sup>+</sup> channels in mammalian brain neurons: Remarkable precision in the midst of extraordinary complexity. *Neuron*, **85**(2), 238–256.
- Wolff, M., Brunklaus, A., & Zuberi, S. M. (2019). Phenotypic spectrum and genetics of SCN2A-related disorders, treatment options, and outcomes in epilepsy and beyond. *Epilepsia*, **60**(S3), 59–67.
- Xiao, Y., Jackson, J. O. 2nd, Liang, S., & Cummins, T. R. (2011). Common molecular determinants of tarantula huwentoxin-IV inhibition of Na<sup>+</sup> channel voltage sensors in domains II and IV. *Journal of Biological Chemistry*, **286**(31), 27301–27310.
- Vogt, K. E., Gerharz, S., Graham, J., & Canepari, M. (2011). Combining membrane potential imaging with L-glutamate or GABA photorelease. *PLoS ONE*, **6**(10), e24911.

## Additional information

### Open research badges



This article has earned an Open Data badge for making publicly available the digitally-shareable data necessary to reproduce the reported results. The data is available at <https://zenodo.org/record/5835995>.

### Data availability statement

The complete dataset of imaging/electrophysiological experiments in brain slices, used in this study, is available in the public repository Zenodo (<https://zenodo.org/record/5835995>). The NEURON model, including the changes of parameters replicating the experiments with hwtx, is available in the NeuronDB database at: <http://modeldb.yale.edu/267355>. Matlab codes used for data analysis are available at <https://github.com/MarcoCanepari/NAV12-BK-paper>.

## Competing interests

The authors declare no conflicts of interest.

## Author contributions

L.F., L.A.B. and M.C. designed the research, L.F. and L.A.B. performed brain slice research and data analysis, J.M. and M.d.W. designed the novel peptide and characterized ion channel selectivity of peptides, L.F. developed the NEURON model and performed computer simulations, and M.C. wrote the paper. All authors have given approval to the final version of the manuscript.

## Funding

Agence Nationale de la Recherche (ANR): Luiza Filipis, Laila Ananda Blömer, Jérôme Montnach, Michel Dewaard, Marco Canepari, ANR-18-CE19-0024; Agence Nationale de la Recherche (ANR): Luiza Filipis, Laila Ananda Blömer, Jérôme Montnach, Michel Dewaard, Marco Canepari, ANR-11-LABX-0015; Agence Nationale de la Recherche (ANR): Marco Canepari, National Infrastructure France Life Imaging; Federation pour la Recherche sur le Cerveau: Marco Canepari, Espoir en tête; Fondation Leducq (Leducq Foundation): Michel Dewaard, N/A.

## Keywords

action potential, axon initial segment, BK Ca<sup>2+</sup>-activated K<sup>+</sup> channel, calcium, Na<sub>v</sub>1.2 channel, neocortical layer-5 pyramidal neuron

## Supporting information

Additional supporting information can be found online in the Supporting Information section at the end of the HTML view of the article. Supporting information files available:

## Statistical Summary Document

## Peer Review History